Draft version February 25, 2022
Typeset using LaTeX **twocolumn** style in AASTeX62

arXiv:2105.06353v1 [astro-ph.EP] 13 May 2021

Longitudinally Resolved Spectral Retrieval (ReSpect) of WASP-43b

Patricio E. Cubillos[1], Dylan Keating[2], Nicolas B. Cowan[2,3], Johanna M. Vos[4], Ben Burningham[5], Marie Ygouf[6], Theodora Karalidi[7], Yifan Zhou[8,9], and Eileen C. Gonzales[10,4,11,12,*]

[1]Space Research Institute, Austrian Academy of Sciences, Schmiedlstrasse 6, A-8042, Graz, Austria
[2]Department of Physics, McGill University, 3600 rue University, Montréal, QC H3A 2T8, Canada
[3]Department of Earth & Planetary Sciences, McGill University, 3450 rue University, Montréal, QC H3A 0E8, Canada
[4]Department of Astrophysics, American Museum of Natural History, 200 Central Park West, New York, NY 10024, USA
[5]Centre for Astrophysics Research, Department of Physics, Astronomy and Mathematics, University of Hertfordshire, Hatfield AL10 9AB, UK
[6]Jet Propulsion Laboratory, California Institute of Technology, Pasadena, CA 91109, USA
[7]Department of Physics, University of Central Florida, 4111 Libra Dr, Orlando, FL, 32816, USA
[8]Department of Astronomy, The University of Texas at Austin, Austin, TX 78712, USA
[9]McDonald Observatory, The University of Texas, Austin, TX 78712, USA
[10]Department of Astronomy and Carl Sagan Institute, Cornell University, 122 Sciences Drive, Ithaca, NY 14853, USA
[11]The Graduate Center, City University of New York, New York, NY 10016, USA
[12]Department of Physics and Astronomy, Hunter College, City University of New York, New York, NY 10065, USA

Abstract

Thermal phase variations of short period planets indicate that they are not spherical cows: day-to-night temperature contrasts range from hundreds to thousands of degrees, rivaling their vertical temperature contrasts. Nonetheless, the emergent spectra of short-period planets have typically been fit using one-dimensional (1D) spectral retrieval codes that only account for vertical temperature gradients. The popularity of 1D spectral retrieval codes is easy to understand: they are robust and have a rich legacy in Solar System atmospheric studies. Exoplanet researchers have recently introduced multi-dimensional retrieval schemes for interpreting the spectra of short-period planets, but these codes are necessarily more complex and computationally expensive than their 1D counterparts. In this paper we present an alternative: phase-dependent spectral observations are inverted to produce longitudinally resolved spectra that can then be fitted using standard 1D spectral retrieval codes. We test this scheme on the iconic phase-resolved spectra of WASP-43b and on simulated *JWST* observations using the open-source Pyrat Bay 1D spectral retrieval framework. Notably, we take the model complexity of the simulations one step further over previous studies by allowing for longitudinal variations in composition in addition to temperature. We show that performing 1D spectral retrieval on longitudinally resolved spectra is more accurate than applying 1D spectral retrieval codes to disk-integrated emission spectra, despite being identical in terms of computational load. We find that for the extant *Hubble* and *Spitzer* observations of WASP-43b the difference between the two approaches is negligible but that *JWST* phase measurements should be treated with longitudinally **re**solved **spect**ral retrieval (ReSpect).

Unified Astronomy Thesaurus concepts: Exoplanet atmospheres (487); Radiative transfer (1335); Spectroscopy (1558); Bayesian statistics (1900)

1. Introduction

Unlike Solar System worlds, short-period planets are poorly modeled by one-dimensional (1D) atmospheric models. Tidal forces tend to lock short-period planets into synchronous rotation with their host star, while the greater incident flux and resulting high temperatures lead to short radiative timescales (Showman & Guillot 2002). As a result, the atmospheric composition—and even phase—can differ qualitatively between a planet's dayside and nightside, e.g., an ultra hot Jupiter will have atomic gas on its dayside and molecular gas on its nightside (Bell & Cowan 2018; Tan & Komacek 2019), while a lava planet has vaporized rock on its dayside but an airless nightside (Léger et al. 2011). Even "modest" temperature contrasts of a few hundred degrees between day and night might lead to first order shifts in chemistry (CH_4 vs. CO; Cooper & Showman 2006; Agúndez et al. 2012) and aerosols (clouds on the nightside, but clear skies on the dayside; Parmentier et al. 2016, 2021; Roman et al. 2021). For relatively cool and rapidly spinning worlds in the Solar System, a 1D "spherical cow" atmospheric model adequately captures the dominant vertical temperature gradients. Short period planets instead need to be considered as at least two-dimensional objects (altitude and longitude). We cannot claim to really understand a short period planet's atmosphere unless we have explained its day-to-night differences.

patricio.cubillos@oeaw.ac.at

* 51 Pegasi b Fellow
LSSTC Data Science Fellow

The most direct way to observe a planet's day-to-night variations in temperature, composition, and aerosols is via phase-curve measurements. Photometric thermal phase variations have been available for more than a decade (Knutson et al. 2007) and enable us to build longitudinal brightness maps (Cowan & Agol 2008) for dozens of hot Jupiters and a few smaller planets (for a recent review see Parmentier & Crossfield 2018). Longitudinal "temperature maps" inferred from photometric phase variations should be interpreted with a grain of salt, however: given the significant changes in composition and aerosols, the opacities can vary dramatically as a function of longitude, so the brightness map in a single band may not represent bolometric flux, nor the temperature along an isobar (Dobbs-Dixon & Cowan 2017). The only way to truly understand the longitudinal variations of a short-period planet are multi-band phase-curve measurements (Knutson et al. 2009, 2012).

Stevenson et al. (2014, 2017) presented 1D spectral retrievals based on disk-integrated spectroscopy of the hot Jupiter WASP-43b at four orbital phases. This approach is not entirely self-consistent, however: 1D spectral retrieval is predicated on a horizontally uniform planet, whereas the time-varying disk-integrated brightness is a testament to the planet's longitudinal inhomogeneity (e.g., Feng et al. 2016; Irwin et al. 2020; Caldas et al. 2019; Taylor et al. 2020). Multidimensional retrievals of the WASP-43b phase-curve data by Irwin et al. (2020) and Feng et al. (2020) have shown significant deviations from previous 1D retrieval results.

1.1. *Thermal-emission Spectral Retrieval for Inhomogeneous Planets*

Recently, there has been a growing interest in performing spectral retrievals for planets with inhomogeneous atmospheres, prompted by the higher quality data that next-generation observatories will provide.

Feng et al. (2016) presented the first exoplanet atmospheric retrievals considering models beyond the 1D assumption. They modeled the planetary flux as a linear combination arising from a "hot" and a "cold" thermal profile component (the components of this 2TP model are averaged and thus represent an observation at quadrature). They showed that the assumption of a single 1D thermal profile biases the retrieved composition of a hot Jupiter atmosphere that is composed of two thermal profiles. When there is a strong day–night temperature contrast, the 1D model overestimated the CH_4 abundance, whereas the two-component model yielded an upper limit, consistent with the input CH_4 abundance. They found a similar result when applying the analysis to the WASP-43b phase-curve data at orbital phase = 0.25.

Irwin et al. (2020) presented "2.5-dimensional" spectral retrievals of WASP-43b using optimal estimation (e.g., Rodgers 2000). They simultaneously fit the disk-integrated spectra at many different orbital phases with an atmospheric model that is a discrete function of longitude and an assumed latitudinal dependence. The number of parameters is therefore proportional to the chosen number of longitudinal slices, $N_l = 16$. Since multiple longitudinal slices contribute to the disk-integrated spectrum at a given phase, each slice is constrained by data from multiple phases. This approach has the advantage of accounting for the different viewing angles for regions near the center of the planetary disk vs. near the limb of the planet—including the poles. Moreover, the atmospheric temperature and composition can vary arbitrarily from one longitudinal slice to the next, which makes this approach very flexible.

Taylor et al. (2020) quantified the impact of performing a 1D spectral retrieval on disk-integrated observations of a horizontally inhomogeneous planet. They note that short-wavelength data are particularly useful at diagnosing a mixture of planetary regions with different temperatures—this is likely a consequence of the stronger temperature-dependence on the Wien than on the Rayleigh-Jeans side of the Planck function (cf. the sum-of-blackbodies of Schwartz & Cowan 2015). The authors first develop an admixture of two 1D models (following Feng et al. 2016) before showing that diluting a single hot temperature–pressure profile with a region that emits no flux whatsoever adequately fits synthetic emission data.

Feng et al. (2020) extended their 2TP approach (Feng et al. 2016) to model a planet's phase curve-emission at any given orbital phase by weighting the intensity from the hot and cold components according to appropriate viewing-geometry corrections. Their analysis of synthetic phase curves of WASP-43b with globally constant composition but inhomogeneous day and night temperature profiles showed that 1D retrievals of simulated 2TP-type planets can significantly overestimate the abundances of species that are absent from the atmosphere (e.g., CH_4). Their analysis of observed WASP-43b phase curves with the 2TP approach tends to favor upper limits for the CH_4 abundance at a few more orbital phases than the 1D approach.

1.2. *Our Approach: Spectral Mapping*

Our approach is complementary to the efforts described above: rather than make the forward model more complex by adding dimensions or atmospheric columns, we opt to process the data one step further than previous researchers. We convert the time-resolved spectra into longitudinally resolved spectra by applying the analytic formalism of Cowan & Agol (2008) at each wavelength. These spectra can then be interpreted with 1D spectral retrieval codes.

It has long been recognized that time-resolved multi-band photometry can be converted to longitudinal maps (e.g., Knutson et al. 2009, 2012), we simply extend this approach to spectral data. In principle, our approach should yield more accurate atmospheric retrievals than the traditional approach of performing 1D spectral retrieval on disk-integrated spectra, while side-stepping the development of higher-dimensional retrieval codes.

In §2 we apply our approach to the iconic spectral phase curve measurements of WASP-43b (Stevenson et al. 2014, 2017) and in §3 to simulated *JWST* observations of the same planet. We discuss our results in §4 and conclude in §5.

2. Atmospheric Retrieval

In this section we retrieve existing spectral phase-curve observations of the hot-Jupiter planet WASP-43b. This study serves multiple purposes. First, it allows us to compare the standard 1D disk-integrated retrieval approach to previous studies from the literature. Second, it allow us to compare the longitudinally resolved retrieval to the disk-integrated approach under current observational capabilities.

2.1. *WASP-43b*

WASP-43b (Hellier et al. 2011) is a highly-irradiated hot-Jupiter planet ($R_{\rm p} = 1.04\ R_{\rm Jup}$, $M_{\rm p} = 2.03\ M_{\rm Jup}$) orbiting a K7 dwarf star ($R_{\rm s} = 0.67\ R_{\odot}$, $T_{\rm eff} = 4520$ K) in a short 19.5 hr orbit (Gillon et al. 2012). These favorable system properties prompted several atmospheric characterization efforts via secondary-eclipse and phase-curve observations. Infrared emission observations during eclipse with the *Spitzer Space Telescope* ruled out the presence of a strong thermal inversion (Blecic et al. 2014), whereas optical observations with the *Hubble Space Telescope* (*HST*) detected the water 1.4 μm feature, consistent with solar-composition values (Kreidberg et al. 2014). Full-orbit phase-curve observations with HST and Spitzer (Stevenson et al. 2014, 2017) suggest a high day–night temperature contrast of ∼1000 K, hence weak heat redistribution, but accompanied by significant emission asymmetry, with phase curves peaking ∼40 minutes before the secondary eclipse. 3D atmospheric circulation models of the planet that exhibit an equatorial superrotating jet that predict the observed eastward-shifted hotspot (Kataria et al. 2015) but not the very low nightside flux that has been contested in subsequent reanalyses of the data (Keating & Cowan 2017; Louden & Kreidberg 2018; Mendonça et al. 2018).

2.2. *Converting Spectral Phase Curves to Longitudinally Resolved Spectra*

The thermal phase variations of an exoplanet are, to good approximation, periodic at the orbital period and hence may be approximated by a Fourier series. Sinusoids turn out to be not only a convenient parameterization for the observed signal, they also lend themselves to analytic conversion between the phase variations and a longitudinal brightness map of the planet (Cowan & Agol 2008; Cowan et al. 2013). Phase-curve mapping suffers from two intrinsic degeneracies: 1) there is nearly no latitudinal information in the phase curves, and 2) certain brightness patterns have no lightcurve signature, a so-called *nullspace* of the transformation (for a review of exoplanet mapping see Cowan & Fujii 2018).

For the WASP-43b disk-integrated dataset, we selected the *HST* WFC3 phase-resolved spectra presented in Table 5 of Stevenson et al. (2017), combined with the broadband *Spitzer* 3.6 μm and 4.5 μm phase curves reanalyzed by Mendonça et al. (2018). We inverted the emission spectra as a function of orbital phase into spectra as a function of planetary longitude by applying the analytic mapping formalism of Cowan & Agol (2008) on the published phase curve parameters. We describe how to analytically estimate maps and their uncertainties for a variety of phase-curve parameterizations in Appendices A, B and C. Without enforcing positive brightness maps, we used a 10,000 iteration Monte Carlo to propagate uncertainties on the published phase curve parameters to the map parameters, and hence the longitudinally resolved spectra themselves.

2.3. *WASP-43b HST+Spitzer Retrieval Setup*

To study the atmosperic properties of WASP-43b we used the open-source PYRAT BAY framework[1] for exoplanet atmospheric modeling, spectral synthesis, and Bayesian retrieval (Cubillos & Blecic 2021). The PYRAT BAY package provides forward- and retrieval-modeling capability, enabling the user to adopt a wide range of custom, self-consistent, or parametric models of the atmospheric temperature, abundance, and altitude profiles. The code can compute emission or transmission spectra considering opacities from molecular line transitions, collision-induced absorption, Rayleigh scattering, gray clouds, and alkali resonance lines. The atmospheric retrieval explores the parameter space via a differential-evolution Markov-chain Monte Carlo sampler (ter Braak & Vrugt 2008), implemented through the open-source code MC3 (Cubillos et al. 2017), and monitors the Gelman & Rubin (1992) statistics for convergence.

We modeled the atmosphere as a set of 61 pressure layers ranging from 100 to 10^{-8} bar. We adopted a parametric temperature profile using the Eddington approximation model (Guillot 2010; Line et al. 2013). We kept fixed the channel partitioning at $\alpha = 0$ and the internal temperature at $T_{\rm int} = 0$ K, which reduces the temperature profile model to $T(p) = T_{\rm irr}\sqrt[4]{\xi(\tau)/4}$, where

$$\xi(\tau) = 2+\frac{2}{\gamma}\left[1+\left(\frac{\gamma\tau}{2}-1\right)e^{-\gamma\tau}\right]+2\gamma\left(1-\frac{\tau^2}{2}\right)E_2(\gamma\tau), \quad (1)$$

with $\tau = \kappa' p$, p the atmospheric pressure, and $E_2(x)$ the second-order exponential integral. The retrieval parameters of this model are thus the irradiation temperature of the planet $T_{\rm irr}$, the visible–thermal ratio of the Planck mean opacities γ, and the thermal Planck mean opacity κ'. For the atmospheric composition we retrieve the volume mixing ratios (X_i) of H_2O, CO, CO_2, and CH_4, assumed to be constant with altitude. The remaining composition is assumed to be H_2, He, and H in solar-abundance ratios under thermochemical equilibrium (Asplund et al. 2009). The altitude profile is computed using the hydrostatic-equilibrium equation, calculated consistently according to the composition (i.e., depending on the mean molecular mass) and temperature of each retrieval sample.

The PYRAT BAY radiative transfer computed the planetary emission spectrum between 1.0 and 5.5 μm, at a constant resolving power of $R = \lambda/\Delta\lambda = 10,000$. To compute the WASP-43 planet-to-star flux ratios we adopted the system parameters from Gillon et al. (2012) and the Kurucz stellar emission model (Castelli & Kurucz 2003) assuming solar metallicity, effective temperature $T_{\rm eff} = 4500$ K, sur-

[1] https://pyratbay.readthedocs.io/

Table 1. PYRAT BAY Atmospheric Retrievals of WASP43b

		Orbital phase 0.25		Orbital phase 0.5		Orbital phase 0.75	
Parameter	Prior	Disk	Resolved	Disk	Resolved	Disk	Resolved
$\log_{10}(\kappa')$	$\mathcal{U}(-7.0, 3.0)$	$-5.4^{+1.5}_{-0.8}$	$-5.5^{+1.4}_{-0.7}$	$-3.4^{+1.1}_{-1.4}$	$-2.8^{+1.1}_{-1.2}$	$-4.2^{+1.6}_{-1.3}$	$-3.8^{+1.6}_{-1.4}$
$\log_{10}(\gamma)$	$\mathcal{U}(-4, 4)$	$-1.1^{+0.4}_{-0.9}$	$-1.0^{+0.4}_{-0.7}$	$-0.9^{+0.4}_{-0.8}$	$-1.1^{+0.5}_{-1.0}$	$-1.3^{+0.6}_{-1.1}$	$-1.4^{+0.6}_{-1.1}$
$T_{\rm irr}$ (K)	$\mathcal{U}(100, 3000)$	1310^{+155}_{-560}	1360^{+125}_{-460}	1300^{+275}_{-490}	1175^{+360}_{-510}	1000^{+260}_{-495}	930^{+280}_{-455}
$\log_{10}(X_{\rm H2O})$	$\mathcal{U}(-12, -1)$	$-4.4^{+1.6}_{-0.4}$	$-4.2^{+1.7}_{-0.4}$	$-2.5^{+0.9}_{-1.0}$	$-2.1^{+0.7}_{-0.8}$	$-3.8^{+1.7}_{-1.0}$	$-3.3^{+1.4}_{-1.2}$
$\log_{10}(X_{\rm CO})$	$\mathcal{U}(-12, -1)$	$-7.4^{+3.9}_{-3.1}$	$-7.4^{+4.0}_{-3.2}$	$-4.6^{+2.7}_{-4.9}$	$-4.7^{+2.8}_{-4.8}$	$-5.4^{+2.9}_{-4.4}$	$-5.0^{+2.8}_{-4.8}$
$\log_{10}(X_{\rm CO2})$	$\mathcal{U}(-12, -1)$	$-8.0^{+3.9}_{-2.8}$	$-7.9^{+4.0}_{-2.8}$	$-5.2^{+1.4}_{-3.6}$	$-5.3^{+1.2}_{-3.5}$	$-4.7^{+2.3}_{-3.5}$	$-4.2^{+2.0}_{-3.8}$
$\log_{10}(X_{\rm CH4})$	$\mathcal{U}(-12, -1)$	$-6.7^{+2.5}_{-3.6}$	$-6.1^{+2.1}_{-3.7}$	$-8.4^{+2.6}_{-2.5}$	$-8.7^{+2.4}_{-2.2}$	$-6.7^{+2.4}_{-3.6}$	$-6.8^{+2.4}_{-3.6}$
$\log_{10}(p_{\rm cloud}/{\rm bar})$	$\mathcal{U}(-6, 2)$	$0.9^{+0.8}_{-0.6}$	$0.8^{+0.8}_{-0.7}$	$0.1^{+1.3}_{-1.3}$	$-0.1^{+1.4}_{-1.4}$	$0.5^{+1.0}_{-1.2}$	$0.4^{+1.1}_{-1.3}$

Notes. The reported retrieved values correspond to the marginal posterior distribution's median and boundaries of the 68% central credible interval (Andrae 2010).

face gravity $\log(g) = 4.5$, and planet-to-star radius ratio of $R_{\rm p}/R_{\rm s} = 0.1596$.

The opacities included the HITEMP line-by-line data for CO (Li et al. 2015) and CO_2 (Rothman et al. 2010), and the ExoMol line-by-line data for H_2O (Polyansky et al. 2018) and CH_4 (Yurchenko & Tennyson 2014). Since the ExoMol line lists consist of several billions of line transitions, we employed the REPACK algorithm (Cubillos 2017) to extract only the main transitions that dominate the absorption spectrum, reducing the number of transitions by a factor of ∼100 (Cubillos 2021, submitted). The model also included collision-induced opacities for H_2–H_2 pairs (Borysow et al. 2001; Borysow 2002) and H_2–He pairs (Borysow et al. 1988, 1989; Borysow & Frommhold 1989); Rayleigh-scattering opacity for H_2 (Lecavelier Des Etangs et al. 2008); and a gray cloud deck parameterized by the cloud top pressure ($p_{\rm cloud}$). Below this pressure level the atmosphere becomes instantly opaque at all wavelengths. Prior to the MCMC run, we sampled the line-by-line opacities into the wavelength and pressure grids of the atmospheric model, as wells as over a temperature array evenly spaced from 100 K to 3000 K with a step of 100 K. Thus, during the MCMC the code only interpolates (linearly) in temperature according to the temperature profile of each iteration.

Table 1 summarizes the retrieval parameterization, priors, and results of our analysis of the Stevenson et al. (2017) and Mendonça et al. (2018) spectra. In addition to these priors, the retrieval also required any temperature value to lie in the range allowed by the opacity data (i.e., 100 K $< T(p) <$ 3000 K), and the atmosphere to have a primary composition (i.e., $\sum X_i < 0.1$, for $i \in \{H_2O, CO, CO_2, CH_4\}$).

2.4. *Comparison to Stevenson et al. (2017) and Mendonça et al. (2018)*

To compare our results with those shown in Fig. 6 of Stevenson et al. (2017), we retrieved both the disk-integrated and longitudinally resolved spectra at three orbital phases: 0.25 (first quarter or Eastern terminator), 0.5 (dayside), and 0.75 (third quarter or Western terminator). Figures 1 and 2 shows our retrieval results.

Our retrieval analysis of the disk-integrated dataset is generally consistent with that of Stevenson et al. (2017). In all cases, the PYRAT BAY models fit the observations well, yielding reduced chi-square values of $\chi^2_{\rm red} = 1.0 - 1.5$. We constrain $X_{\rm H2O}$ at all three phases, obtaining higher abundances for the dayside spectrum. At first and third quarters, H_2O shows a main solution mode in the $10^{-5} < X_{\rm H2O} < 10^{-4}$ range. For this mode, the mixing ratios of the three other molecules are not strongly correlated with $X_{\rm H2O}$, and show mostly low values (see Fig. 2). Additionally, the $X_{\rm H2O}$ posterior shows a tail of higher values that are strongly correlated with $X_{\rm CO}$, $X_{\rm CO2}$, and $X_{\rm CH4}$, and anti-correlated with $p_{\rm cloud}$. The strongest CH_4 absorption band is probed by the *Spitzer* 3.6-μm filter, thus, this data point (relative to the *HST* observations) mainly determines the $X_{\rm CH4}$ posterior distribution. The $X_{\rm CH4}$ posteriors show mostly upper-limit constraints, being more stringent at the dayside phase ($X_{\rm CH4} \lesssim 6$), and allowing for higher values at the first- and third-quarter phases ($X_{\rm CH4} \lesssim 4$). In contrast, Stevenson et al. (2017) find tighter constraints at $X_{\rm CH4} \approx 10^{-4}$. This discrepancy is not surprising, since we adopted the *Spitzer* data reanalyzed by Mendonça et al. (2018), which exhibits higher planetary emission at 3.6 μm (which contains the strongest CH_4 band probed by these observations) than Stevenson et al. (2017). For a non-inverted temperature profile, a stronger planet-to-star flux ratio implies that there is less atmospheric absorption such that the observations probe deeper, hotter layers. To reduce the absorption, the model thus requires a lower concentration of the dominant absorber, in this case CH_4.

Analogously to CH_4, the strongest absorption bands for CO and CO_2 are probed by the *Spitzer* 4.5-μm channel. This broadband datum cannot distinguish CO from CO_2 absorption, leading to anti-correlated $X_{\rm CO}$–$X_{\rm CO2}$ posteriors. Compare for example the spectra at first and third quarters, since the 4.5 μm eclipse depth at phase 0.75 is much lower than at phase 0.5, the data drive the posterior distribution towards higher $X_{\rm CO}$ or $X_{\rm CO2}$ values (higher abundances increase the absorption at high altitudes, where it is colder for a non-

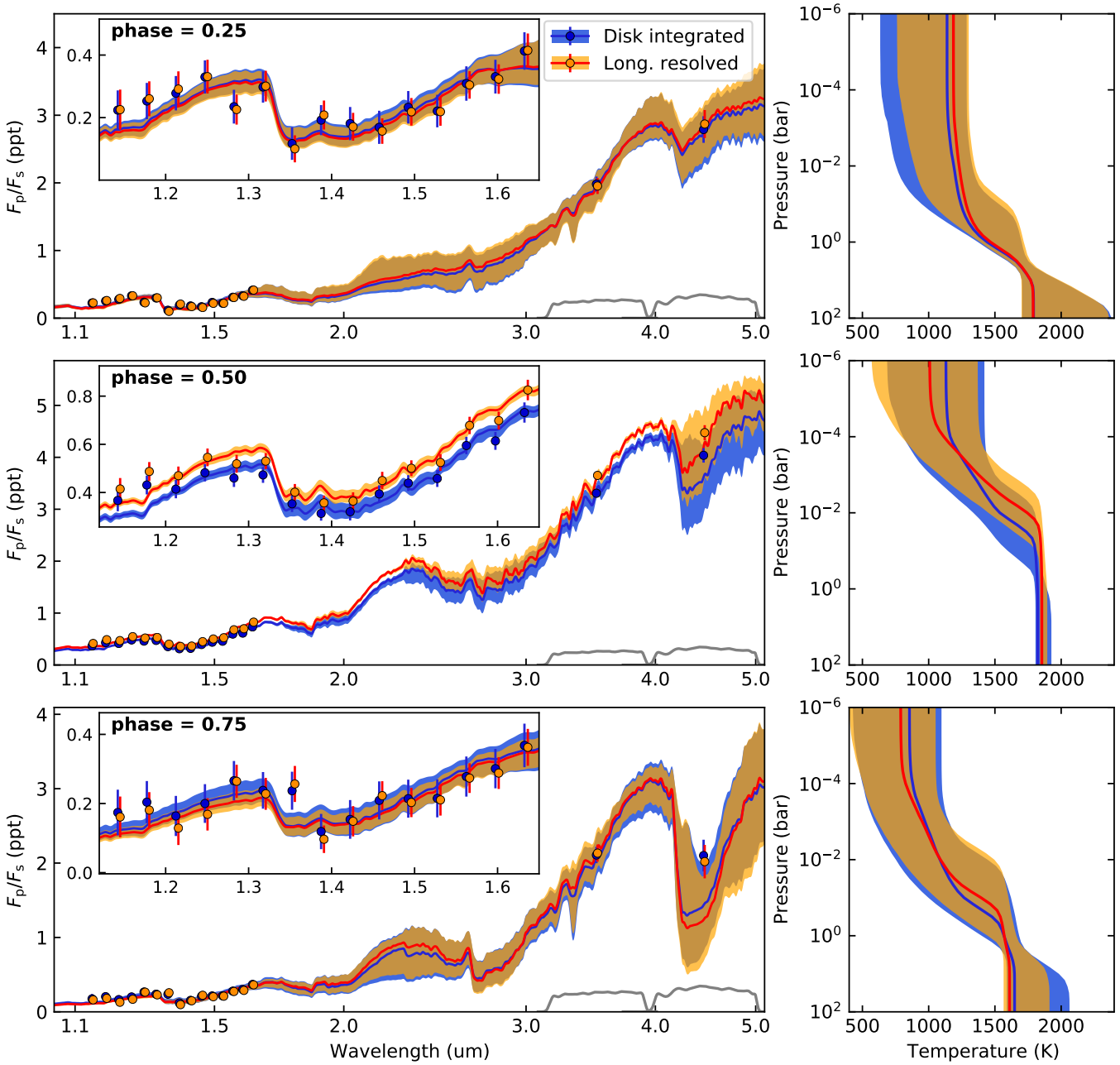

Figure 1. WASP-43b retrieval with PYRAT BAY of the Stevenson et al. (2017) and Mendonça et al. (2018) spectra at orbital phases of 0.25 (top), 0.5 (middle), and 0.75 (bottom). All panels follow the same color coding, where blue and orange colors correspond to the disk-integrated and longitudinally resolved analyses, respectively. The solid curves and shaded areas denote the median and 68% credible interval of the posterior distributions for the spectra (left panels) and temperature profiles (right panels). The colored markers with error bars show the datasets being fit (left panels). The longitudinally resolved data points have been slightly shifted in wavelength for better visibility. The inset panels zoom in on the wavelengths observed by *HST*.

inverted temperature profile, and hence produce lower planetary emission). At the dayside phase, X_{CO}/X_{CO2} posteriors prefer large values to overcome the H_2O absorption at 4.5-μm absorption. The pair-wise posteriors favor runs with a certain minimum amount of X_{CO}, X_{CO2}, or both (right-bottom set of panels in Fig. 2).

Our temperature posteriors are consistent with those of Stevenson et al. (2017) as well, showing non-inverted temperature profiles in the ∼1000–1800 K range, with photospheres concentrated near 10–10^{-3} bar. Finally, we ran cloud-free retrievals to study the impact of the cloud model. The models are able to fit the data equally well with or without the gray cloud model. Both cloudy and cloud-free modeling yield similar results in terms of chemistry and temperature. The Bayesian information criterion (BIC, Schwarz 1978) therefore favors the simpler cloud-free model.

2.5. *Longitudinally Resolved Retrieval Results*

We found that the longitudinally resolved spectra at first and third quarters are practically indistinguishable from the

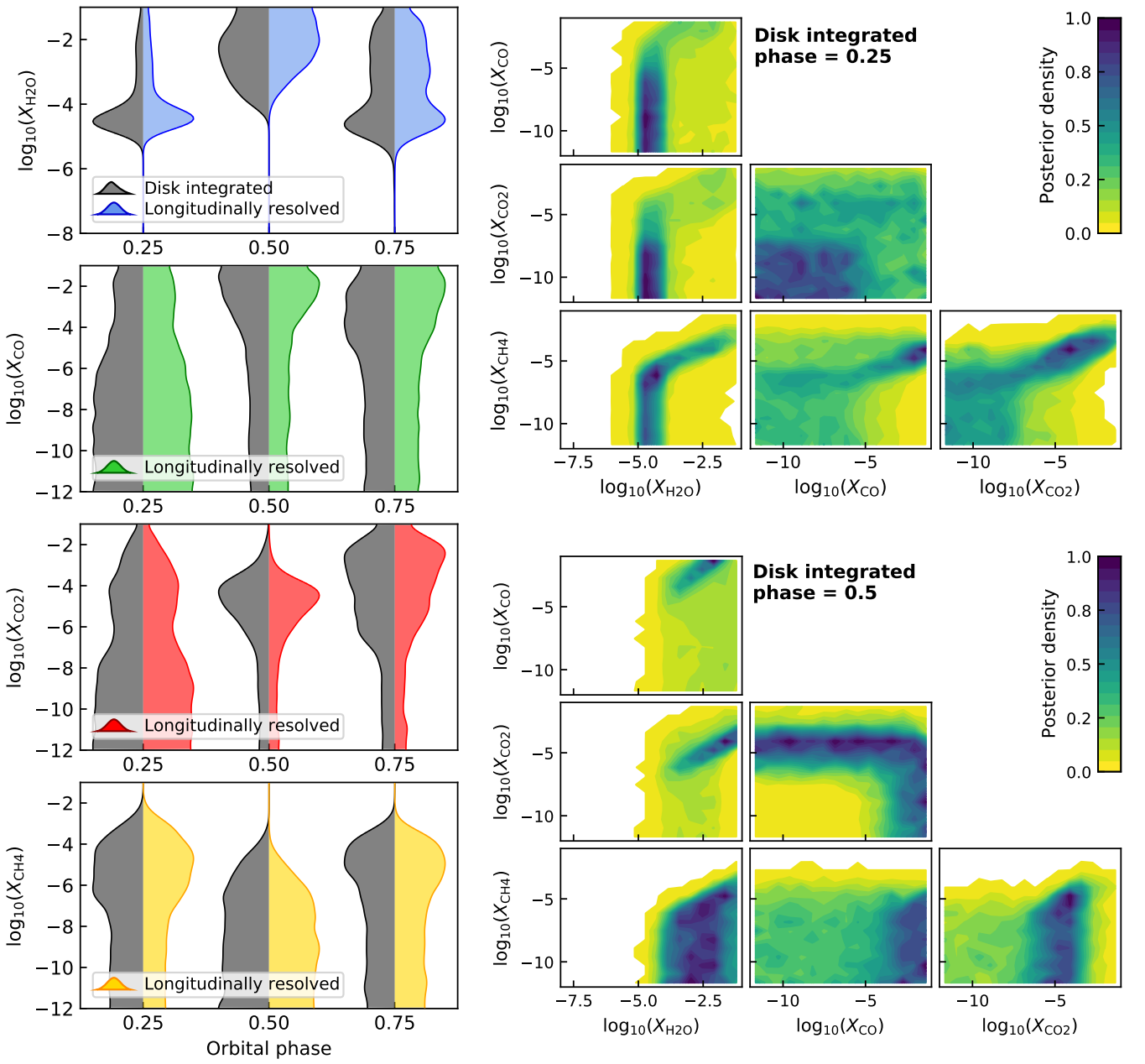

Figure 2. Retrieved WASP-43b volume-mixing ratios of the Stevenson et al. (2017) and Mendonça et al. (2018) phase-curve spectra. The left panels show the abundance marginal posterior distributions for the longitudinally resolved (colored) and disk-integrated (gray) analyses at the three orbital phases shown in Fig. 1. The marginal posteriors have been smoothed for better visualization. The sets of panels on the right show two examples of the abundance pair-wise posterior distributions at orbital phases of 0.25 (top panels) and 0.5 (bottom panels) of the disk-integrated analysis.

disk-integrated spectra (the differences are smaller than the uncertainties, Figs. 1 and 2). Consequently, the longitudinally resolved retrieved results are nearly identical to those of the disk-integrated spectra.

For the dayside phase, the longitudinally resolved spectrum is brighter than the disk-integrated spectrum at all wavelengths, which is expected, since this phase is located near the peak of the phase curve and the conversion to longitudinally resolved spectra acts as a low pass filter. Consequently, the retrieval analysis found a temperature profile that remains hotter at higher altitudes compared to the disk-integrated profile (Fig. 1, middle panels). In terms of composition, the $X_{\rm CO}$, $X_{\rm CO2}$, and $X_{\rm CH4}$ posterior distributions are consistent with the disk-integrated posteriors. Only the $X_{\rm H2O}$ posterior is noticeably shifted to higher values, although the medians of the longitudinally resolved and disk-integrated posteriors are not statistically different (Table 1).

These results suggest that, given the available *HST* and *Spitzer* phase-curve observations of WASP-43b, the longitudinally resolved analysis allows us to detect a hotter temperature of the planet around its substellar point (day-side phase), than that inferred from a disk-integrated analysis. However,

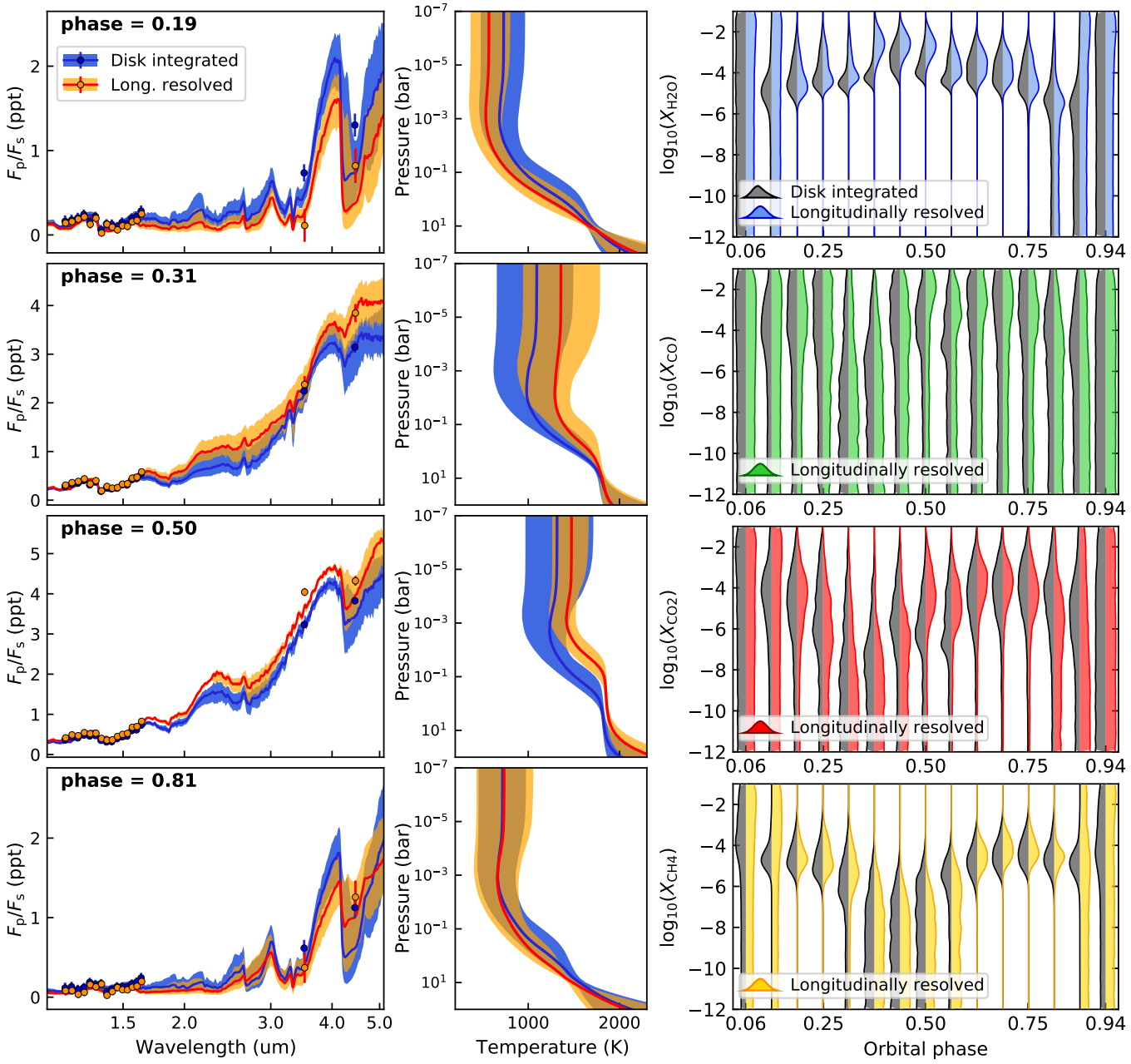

Figure 3. WASP-43b retrieval with PYRAT BAY of the Stevenson et al. (2017) phase-curve spectra, following the atmospheric parameterization of Feng et al. (2020). The left and center panels shows the retrieved spectra and temperature profiles at selected phases (see labels) from top to bottom. The solid curves and shaded areas denote the median and 68% credible interval of the posterior distributions for the disk-integrated (blue colors) and longitudinally resolved (orange colors) analyses. The colored markers with error bars show the datasets being fit (left panels). The right panels show the abundance marginal posterior distributions for the disk-integrated (gray) and longitudinally resolved (colored) analyses as a function of orbital phase. The marginal posteriors have been smoothed for better visualization.

the data do not have sufficient signal-to-noise to detect spectral variations. Therefore, the atmospheric composition estimated from the longitudinally resolved analysis does not differ significantly from that of the disk-integrated analysis.

2.6. *Comparison to Feng et al. (2020)*

To put the results of the longitudinally resolved retrieval approach in context with other multi-dimensional retrieval approaches, we compared our the WASP-43b retrieval analysis to those of Feng et al. (2020).

We retrieved the WASP-43b phase-curve spectra at the 15 orbital phases reported by Stevenson et al. (2017) and, in contrast to our previous analysis, we fit the Stevenson et al. (2017) for both *HST* and *Spitzer* rather than fitting the Mendonça et al. (2018) *Spitzer* data. We adopted the same system properties and atmospheric parameterization of Feng et al. (2020). For the temperature profile we employed the Edding-

ton approximation temperature profile with all five parameters free, using their priors. For the composition, we assumed a cloud-free atmosphere and fit for the H_2O, CO, CO_2, and CH_4 volume mixing ratios (neglecting NH_3 since it does not impact the observed spectra).

Figure 3 shows our retrieval results. In terms of the 1D disk-integrated analysis, our composition posterior distributions follow the same trends with orbital phase for all four molecules as those of Feng et al. (2020). The low flux at the night side leads to unconstrained composition for all molecules for the 2–4 phases near the anti-stellar point. The H_2O composition is constrained at all other phases at values $X_{\rm H2O} \sim 10^{-4}$, and generally increasing toward the hot-spot longitude (phase ∼0.45). $X_{\rm CO}$ is unconstrained, whereas $X_{\rm CO2}$ is largely unconstrained except at some phases after secondary eclipse. For CH_4 we found well-constrained abundances around both quadratures at $X_{\rm CH4} \sim 10^{-5}$ and upper limits around the hot-spot longitude.

Regarding the longitudinally resolved analysis, the retrieved compositions remained largely consistent with those of the disk-integrated analysis. The longitudinally resolved $X_{\rm H2O}$ posteriors have somewhat higher values at certain phases (similar to Feng et al. 2020) and the $X_{\rm CH4}$ posteriors show only modest differences with respect the disk-integrated posteriors (three well-constrained posteriors turned to upper limits). In comparison, the 2TP approach of Feng et al. (2020) found more distinct differences in the CH_4 posteriors. Out of the eight orbital phases with well-constrained $X_{\rm CH4}$ by their 1D model, the 2TP approach favored upper limits at four phases. At the remaining phases, the 2TP $X_{\rm CH4}$ posteriors peaked near their 1D counterparts, although with lower precision (see Fig. 6 of Feng et al. 2020).

Conceptually, the temperature profiles of Feng et al. (2020) and our approaches are widely different; while ours represents the local profile at a specific longitude on the planet, theirs represents the profiles of hot and cold components. Thus, we cannot make a direct comparison between these approaches. However, generally, the two approaches obtained similar non-inverted profiles along the orbit, ranging from ∼500 K to 1500 K between the night side and day side.

While the study of Feng et al. (2020) indicates that the 2TP approach can effectively recover more accurate physical properties under the assumption of a two-component atmospheric model, it is not possible to assess which approach is more accurate without knowing a ground truth. In the next section we aim to characterize the validity of the longitudinally resolved approach by retrieving synthetic phase curve spectra of atmospheric models that are more sophisticated than in previous studies found in the literature.

3. Retrieval of Synthetic *JWST* WASP-43b Phase-curve Spectra

We hypothesize that observations with greater constraining power than the *HST* and *Spitzer* observations of WASP-43b would benefit more from the use of longitudinally resolved spectral retrieval. To test this hypothesis, we performed atmospheric retrievals of synthetic WASP-43b phase-curve observations with the upcoming *James Webb Space Telescope* (*JWST*).

3.1. *Two Inhomogeneous Models of WASP-43b*

We based the inhomogeneous planetary models on the WASP-43b 3D global circulation model (GCM) of Venot et al. (2020), which we analyzed with both the disk-integrated and longitudinally resolved approaches. The GCM solves a coupled system of radiative-transfer and primitive equations on a cube-sphere grid, considering the incident stellar irradiation of WASP-43 and equilibrium molecular abundances for a cloudless solar-composition model. The uneven stellar forcing produces a large day–night temperature contrast of ∼600–800 K at photospheric pressures (∼1 bar to 1 mbar). Strong zonal winds lead to an equatorial superrotation regime and a hotspot shifted eastward of the sub-stellar point. Thus, phase-curve observations generated from this GCM have a peak infrared flux that occurs before secondary eclipse (see also Kataria et al. 2015).

The GCM consists of a 3D grid of temperatures in terms of latitude (θ), longitude (ϕ), and pressure (p). The latitude and longitude grids are linearly spaced over the planet with 32 and 64 samples, respectively. The pressure profile is logarithmically spaced between 170 bar and 3×10^{-6} bar with 52 samples. The longitude origin is located at the sub-stellar point and increases eastward. In this scheme, the planet rotates along the Z axis; the orbital phase increases from 0.0 (nightside facing the observer, transit), to 0.5 (dayside facing the observer, eclipse), to 1.0 (nightside facing the observer, transit). Note that in the Appendices the orbital phase is measured in radians and with the origin at eclipse midtime.

In our framework, we kept the 32×64 latitude–longitude grid, but to simplify the interpretation of the retrieval analysis, we divided the planet into 16 longitudinal slices, where all grid cells in a given slice have the same vertical temperature and composition profiles (Figure 4, top–left panel). We assumed a circular orbit with 90° inclination and zero obliquity.

We computed the temperature profile for each slice by selecting a set of GCM profiles evenly spaced in longitude and at a latitude of 30°S. We fit these temperature profiles with the Madhusudhan & Seager (2009) parametric temperature model. This model divides the atmosphere into three regions, delimited by pressures p_1 and p_3:

$$T(p) = \begin{cases} T_0 + \left[\frac{1}{a_1}\ln(p/p_0)\right]^2 & \text{if } p < p_1 \quad \text{(layer 1)} \\ T_2 + \left[\frac{1}{a_2}\ln(p/p_2)\right]^2 & \text{if } p_1 \leq p < p_3 \quad \text{(layer 2)} \\ T_3 & \text{if } p \geq p_3 \quad \text{(layer 3)} \end{cases} \tag{2}$$

with T_0 the temperature at the top of the atmosphere (p_0), and parameters a_1, a_2, and p_2 controlling the variation of temperature with pressure (T_2 and T_3 can be derived by evaluating the model at the layers' boundaries). During this fitting step, we resampled the profile into our 100–10^{-8} bar pressure range from §2.3, and turned small thermal inversions

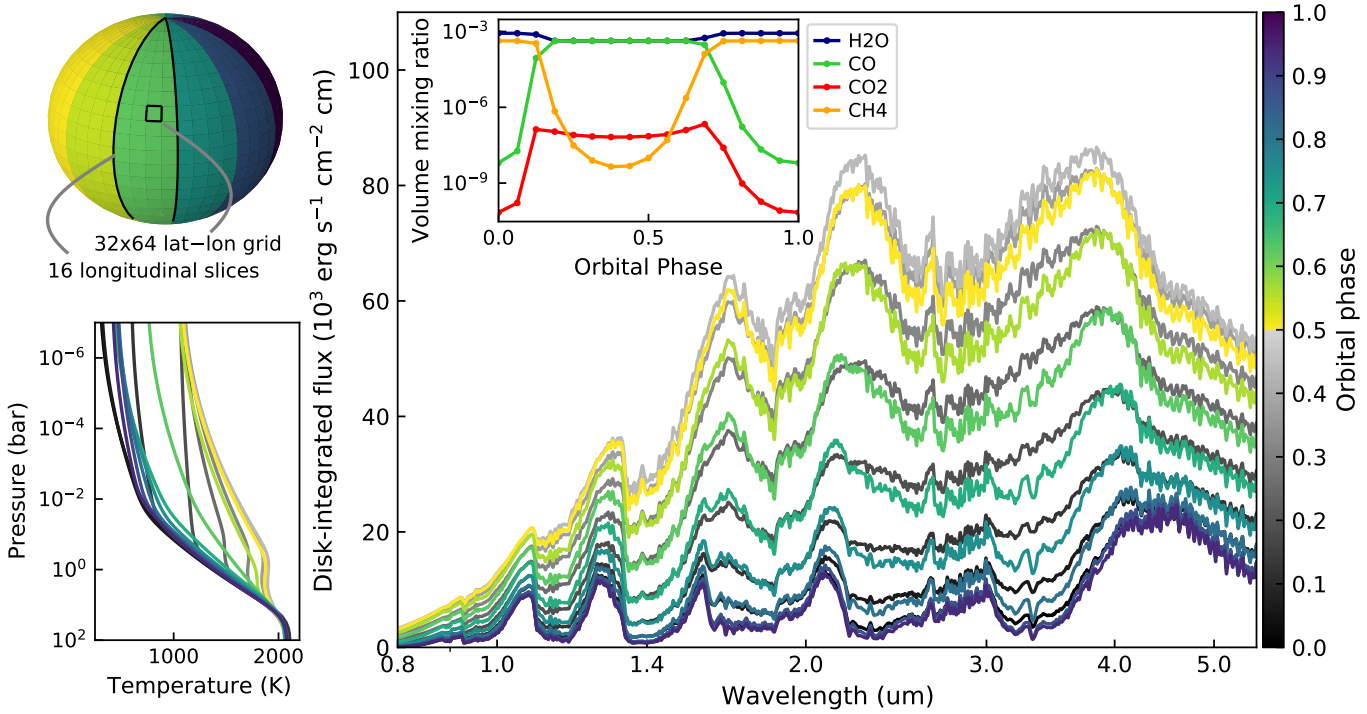

Figure 4. Synthetic WASP-43b model. The sketch on the top left depicts the partitioning of the planetary model (16 longitudinal slices, each with a uniform temperature profile and composition). The bottom left panel shows the temperature profile of the 16 slices color coded by orbital phase (color bar on the far right). The right panel shows the disk-integrated emission spectra as observed at 16 phases along the orbit. The inset shows the volume mixing ratios of the spectroscopically active molecules.

near the 1-bar level into isothermal regions (Fig. 4, bottom–left panel).

We considered two levels of complexity for the atmospheric model (Table 2). The simpler case (M1) assumed a symmetric day-to-night temperature profile variation for the 16 longitudinal slices by adopting the 9 temperature profiles of the evening side, folding them over the entire orbit symmetrically around the hottest profile placed at secondary eclipse (see viridis color-mapped profiles in Fig. 4). For the composition we assumed globally constant abundances adopting the values from Feng et al. (2020), i.e.: $X_{\rm H2O} = 4 \times 10^{-4}$, $X_{\rm CO} = 2 \times 10^{-4}$, and $X_{\rm CO2} = X_{\rm CH4} = 10^{-9}$.

Table 2. Synthetic WASP-43b Models

Model	Temperature Profile	Composition
M1	day–night symmetric	globally constant
M2	asymmetric, hot-spot offset	varying with longitude

For the more complex case (M2), we adopted the 16 asymmetric temperature profiles derived from the GCM (Fig. 4). We adopted a cloud-free solar elemental composition with vertically uniform volume mixing ratios but varying with longitude. Although the vertically uniform assumption clearly deviates from self-consistent chemical or radiative prescriptions, at present this is a common assumption for exoplanets. The use of more sophisticated models is impractical for exoplanet retrievals since they show a higher complexity than what can be constrained by observations and have higher computational demands than simpler parametric models. Furthermore, the limited spectral range of the observing instruments limits the pressure range of the atmosphere being probed. We considered the opacity of H_2 and He (dominant gases), and H_2O, CO, CO_2, and CH_4 (trace gases). To compute the composition at each longitudinal slice, we calculated thermochemical-equilibrium abundances using the open-source code RATE (Cubillos et al. 2019), evaluated at the temperatures near the 0.1-bar level. This choice leads to a well-defined transition between CH_4 and CO/CO_2 trace gases between the night side and the day side (Fig. 4, inset). We did not take into account reflected light, which could be significant in the near infrared (Keating & Cowan 2017).

To generate the phase-curve emission spectra we followed the procedure of Blecic et al. (2017). We computed the disk-integrated spectra as the sum of the intensities from each latitude–longitude cell, weighted by their projected area in the direction of the observer:

$$F_\lambda(\xi) = \sum_{\theta,\phi} I_\lambda(\theta,\phi,\xi)\ \mu(\theta,\phi,\xi)\ \Delta A(\theta,\phi), \qquad (3)$$

where, for each cell, the surface element is $\Delta A(\theta,\phi) = \sin\theta \Delta\theta\Delta\phi$, and the angle from the normal vector is $\mu(\theta,\phi,\xi) = \sin\theta\cos(\phi - \phi_\xi)$, with ϕ_ξ the sub-observer longitude at orbital phase ξ. Note that Eq. (3) sums only over the cells in the hemisphere visible to the observer, i.e., $\mu > 0$. Under the local-thermodynamic-equilibrium and plane-parallel approximations, the emergent intensity spec-

trum is given by

$$I_\lambda(\theta,\phi,\xi) = \int_0^{\tau_{\rm max}} \frac{1}{\mu} B_\lambda(\tau) e^{-\tau/\mu} {\rm d}\tau, \quad (4)$$

where B_λ is the Planck function, and $\tau = \tau_\lambda$ is the optical depth, which is integrated from the top of the atmosphere ($\tau_\lambda = 0$) to the bottom ($\tau_\lambda = \tau_{\rm max}$). Figure 4 (right panel) shows the WASP-43b disk-integrated model spectra evaluated at 16 phases along the orbit. These models consider the same wavelength sampling and opacities sources as in §2.3, but range from 0.8 to 5.5 μm.

Note that since the underlying GCM input has an equatorial jet that transports energy eastward (Kataria et al. 2015), the phase curve is characterized by a hot-spot offset (peak emission occurs near phase 0.44, slightly before secondary eclipse) and an asymmetric variation (the observed spectrum 'heats up' faster than it 'cools down' around the hot spot). This asymmetry has clear repercussions in the composition, for example, the methane feature at 3.4 μm (Fig. 4, right panel) is more prominent at the evening phases (0.5–1.0) than at the morning phases (0.0–0.5). Our setup is distinctly more complex than other recent multi-dimensional atmospheric retrieval studies, which only vary the temperature profile with longitude while keeping a globally homogeneous composition; however, we believe that this is necessary to better capture the complexity of exoplanet atmospheres, and to prevent arriving at overly optimistic results.

3.2. *Simulated JWST Observations*

We modeled expected *JWST* performance using the PANDEXO interface (Batalha et al. 2017) to the *JWST* Exposure Time Calculator[2] (Pontoppidan et al. 2016). We selected the NIRISS SOSS and NIRSpec G395H instruments since they provide a nearly complete coverage from 0.8 to 5.2 μm with only two instruments, and better signal-to-noise ratios than alternative instruments (NIRSpec PRISM could cover the entire 0.8–5.0 μm range in a single observation but with notably lower signal-to-noise ratios). We followed the same assumptions as Venot et al. (2020) to estimate the observing times, i.e., we observe each phase for 1/16th of the orbital period with a baseline of twice the eclipse duration. We let PANDEXO optimize the exposure parameters, reaching 80% of the detector's maximum saturation level. We assumed a stellar K-band magnitude of 9.27, based on the Kurucz model of the star.

For NIRISS SOSS, we selected the GR700XD disperser, SUBSTRIP96 subarray and NISRAPID readout pattern (0.8–2.8 μm range), with a noise floor of 20 ppm, following the expected instrumental noise level (Greene et al. 2016). This yields 113 integrations of 38 groups for each orbital phase, leading to a SNR of 5900 at 1.5 μm. For NIRSpec, we selected the G395H grating, S1600A1 fixed slit, SUB2048 subarray, and NRSRAPID readout pattern (2.9–3.7 μm and 3.8–5.2 μm ranges), with a noise floor of 30 ppm, as well as the aperture spectral extraction strategy, with a target aperture of 0.75 arcsec, and a sky band ranging from 0.75 to 1.5 arcsec. This yields 95 integrations of 18 groups for each orbital phase, leading to a SNR of 430 at 4 μm. The *JWST* Exposure Time Calculator reported no warnings nor errors for any of these calculations.

We adopted as the disk-integrated dataset the model described in the previous section, which we binned to a resolving power of $R \approx 200$ and propagated the PANDEXO uncertainties accordingly. We did not add random noise to the data points (following suite with, Feng et al. 2018; Mai & Line 2019; Taylor et al. 2020), such that we can attribute any inaccuracy of the retrieval to the methodology rather than to statistical random sampling from the true model. A side effect of this choice is that we no longer expect the $\chi^2_{\rm red}$ to approach unity. We constructed the longitudinally resolved datasets by fitting a Fourier series to the simulated disk-integrated spectra and repeating the procedure of §2.3.

To determine the appropriate order of Fourier series for fitting the simulated data, we fit several series of sinusoids to the simulated WASP-43b phase curves at each wavelength, from first order to fourth order. We used PyMC3 (Salvatier et al. 2016) to fit the data and estimate uncertainties. For each model, we calculated the Widely Applicable Information Criteria (WAIC; Watanabe 2010) for each model. The WAIC is similar to the BIC, but uses the full fit posteriors. The second order model was favoured over the other models, meaning we can detect first and second order modes but are insensitive to higher orders. At each step of the MCMC, we calculated the wavelength-dependent longitudinal brightness maps and associated uncertainties.

We analyzed the synthetic data in the same manner as the *HST+Spitzer* observations, except that in this case we assumed a cloud-free atmosphere and used the Madhusudhan & Seager (2009) temperature-profile parameterization (same model parameterization as that used to construct the input model). Table 3 summarizes the model parameterization for the synthetic *JWST* WASP-43b retrievals.

Table 3. Synthetic *JWST* WASP-43b Retrieval Parameterization

Parameter	Priors
$\log_{10}(p_1/{\rm bar})$	$\mathcal{U}(-7,2)$
$\log_{10}(p_2/{\rm bar})$	$\mathcal{U}(-7,2)$
$\log_{10}(p_3/{\rm bar})$	$\mathcal{U}(-5,2)$ and $p_3 > p_1$
a_1 ($\rm K^{-0.5}$)	$\mathcal{U}(0,2)$
a_2 ($\rm K^{-0.5}$)	$\mathcal{U}(0,2)$
T_0 (K)	$\mathcal{U}(100,3000)$
$\log_{10}(X_{\rm H2O})$	$\mathcal{U}(-12,-1)$
$\log_{10}(X_{\rm CO})$	$\mathcal{U}(-12,-1)$
$\log_{10}(X_{\rm CO2})$	$\mathcal{U}(-12,-1)$
$\log_{10}(X_{\rm CH4})$	$\mathcal{U}(-12,-1)$

[2] https://jwst.etc.stsci.edu/

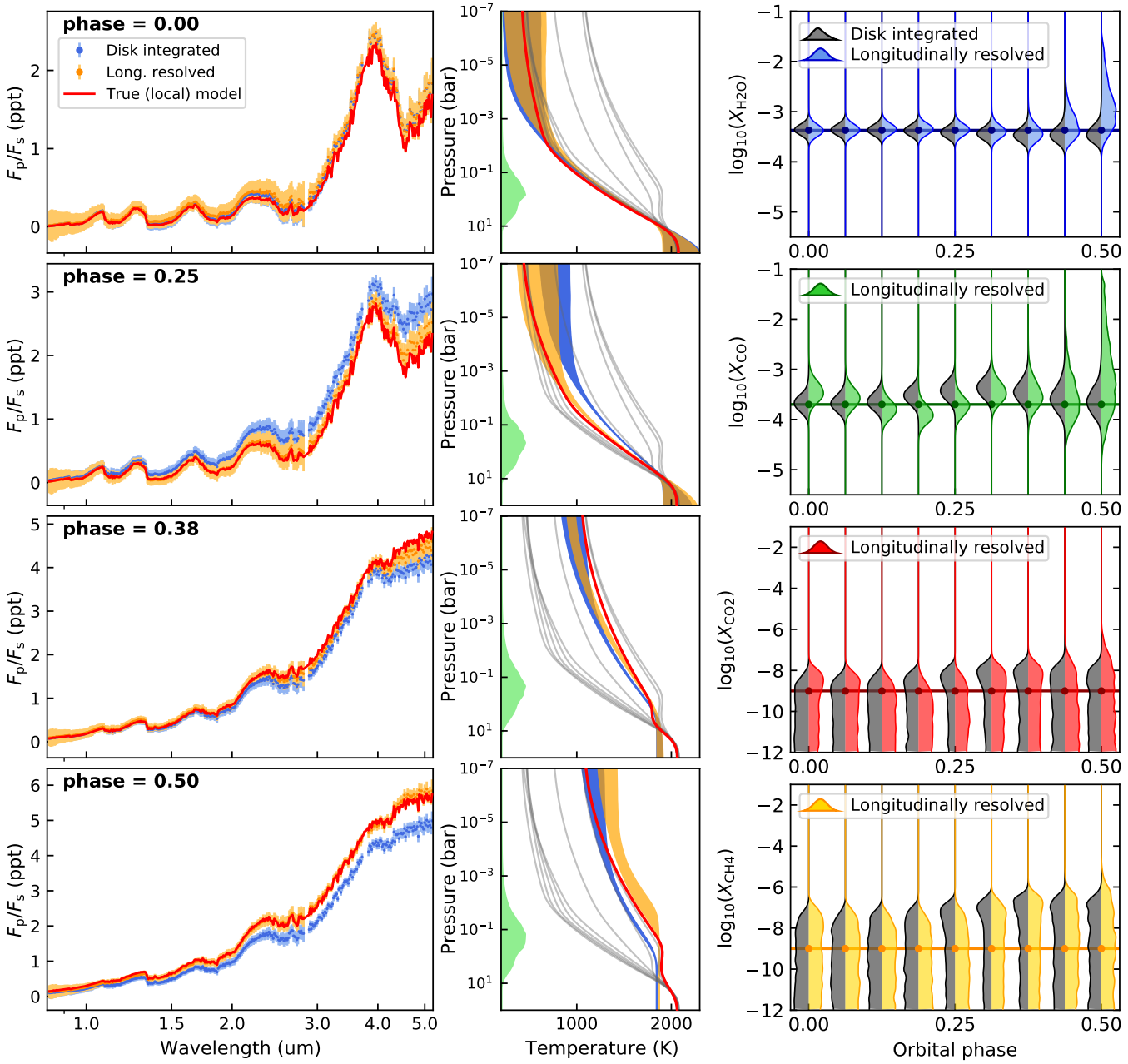

Figure 5. Model and retrieval of the synthetic WASP-43b *JWST* phase-curve observation of the constant-composition case (M1). **Left panels:** the markers with error bars denote the disk-integrated (blue) and longitudinally resolved (orange) planet-to-star flux ratios at selected phases (from top to bottom, see labels). The red curves denote the spectra generated from a 1D model using the local conditions of the true model at the sub-observer longitude of each orbital phase. **Center panels:** retrieved temperature profiles of the synthetic datasets from the left panel. The blue and orange shaded areas denote the disk-integrated and longitudinally resolved temperature-profile posterior distributions, respectively (central 68% credible interval of the posteriors). The red curves denote the temperature profile at the sub-observer longitude of each phase. The gray curves denote the temperature profiles of the true model at all other longitudinal slices. The width of the green curve denotes the relative contribution function at each pressure level for these *JWST* simulations. **Right panels:** volume-mixing-ratio posterior distributions for the disk-integrated (gray) and longitudinally resolved (colored) analyses as a function of orbital phase (only shown between transit and eclipse epoch, since the model is symmetric). The marginal posteriors have been smoothed for better visualization. The solid curves with dot markers denote the abundances of the true model.

3.3. *Retrieval of Synthetic WASP-43b Phase Curve with Constant Composition (M1)*

Figure 5 (left panels) show a sample of the synthetic disk-integrated and longitudinally resolved spectra. This figure also shows 1D model spectra assuming the local properties at the corresponding sub-observer longitude of each phase. Unlike the *HST*/*Spitzer* spectra, the simulated *JWST* datasets show significant differences between the disk-integrated and longitudinally resolved spectra, which are both phase- and wavelength-dependent. At all phases the longitudinally resolved spectra reproduce better the local spectra of the respective sub-observer longitudes, particularly near quadrature (phases 0.25) and secondary-eclipse epoch (phase 0.5).

The retrieved temperature profiles follow the same trend as the spectra, with the longitudinally resolved profiles matching the local profiles better than the disk-integrated profiles. Over the 10–10^{-3} bar region probed by the observations the longitudinally resolved retrieval always reproduces the local temperature of the planet, whereas the disk-integrated retrieval can miss the true temperatures by up to $\sim$100 K (many times the credible intervals). The magnitude of this mismatch is consistent with the mismatch in the spectra at the respective orbital phases.

In terms of composition, the disk-integrated analysis retrieves the true values within the posterior credible intervals (constraining the H_2O and CO volume-mixing ratios and finding upper limits for CO_2 and CH_4). The longitudinally resolved analysis produces similar results, well in agreement with the true values as well.

3.4. *Retrieval of Synthetic WASP-43b Phase Curve with Variable Composition (M2)*

Figure 6 (left-side panels) shows a sample of the synthetic disk-integrated (blue), longitudinally resolved (orange), and true model at the local sub-observer longitude (red) spectra. Once again, the simulated *JWST* datasets show significant differences between the disk-integrated and longitudinally resolved spectra.

Both the disk-integrated and longitudinally resolved retrievals fit the data (not shown); however, the longitudinally resolved spectra give a more accurate representation of the local spectra. Overall, the spectra are more uniform on the night side than on the day side: the disk-integrated and longitudinally resolved spectra are consistent with each other at the longitude opposite the hot-spot (phase = 0.94). At the surrounding longitudes, the disk-integrated spectra overestimate the local planetary emission because of the contribution from the hotter dayside flux contributing to the observed hemisphere. Around the hot-spot longitude we have the opposite situation, the disk-integrated spectra underestimate the local planetary emission since the hemispheric integration dampens the signal. The longitudinally resolved spectra provide a much better match to the local spectra at all phases.

Figure 6 (right-side panels) shows the retrieved temperature-profile posteriors at selected orbital phases. The simulated observations probe mainly between 10^{-3} and 10 bar as shown by the contribution functions (green curves), and thus the upper and lower end of the profiles are an extrapolation of the parametric profiles. We found that the longitudinally resolved temperature posteriors are much more consistent with the true temperature profiles than the disk-integrated posteriors at most orbital phases (the longitudinally resolved fits are sometimes on par with the disk-integrated, but never worse).

Figure 7 shows the retrieved volume-mixing ratios as a function of orbital phase. Each of the four molecules is spectroscopically detectable at least during some orbital phases, though not all simultaneously. Given the assumed pseudo-thermochemical equilibrium chemistry of the input model, CH_4 is abundant and hence detectable at the cooler night-side longitudes at the expense of CO and CO_2; as one approaches the hot spot, CH_4 turns into CO and CO_2 due to the higher temperature, making CO and CO_2 detectable at the dayside longitudes. As expected, the $X_{\rm H2O}$ constraint was the most accurate and precise of the four molecules. The longitudinally resolved post processing seemed to have lowered the accuracy and precision at specific phases, but the posteriors still capture the true value within the 68% credible intervals. Possibly, the high abundance and weak variation of $X_{\rm H2O}$ along the orbit helps the retrievals to fit this molecule more accurately.

In contrast, $X_{\rm CO}$ and $X_{\rm CO2}$ vary significantly along the orbit. At the dayside longitudes, $X_{\rm CO}$ and $X_{\rm CO2}$ are well-constrained since CO and CO_2 are abundant enough to show detectable spectral features. At the night-side longitudes, the CO and CO_2 abundances drop below detectable levels, leading to upper-limit posteriors for $X_{\rm CO}$ and $X_{\rm CO2}$. The longitudinally resolved $X_{\rm CO}$ and $X_{\rm CO2}$ posteriors are in good agreement with the true local values at nearly all phases (i.e., within the 68% credible interval). The disk-integrated $X_{\rm CO}$ and $X_{\rm CO2}$ posteriors also trace the behavior of the true values, but perform particularly poorly near first- and third-quarter phases. A possible explanation could be that these are the phases where the abundances vary the most across the visible hemisphere. Considering that the abundance estimations are strongly correlated between the different species, and that the strength of the spectral features do not scale linearly with the abundances, biases propagate particularly strongly at these highly heterogeneous phases.

The CH_4 retrieval showed the poorest results. At the night-side longitudes, $X_{\rm CH4}$ remains abundant and constant. Both disk-integrated and longitudinally resolved $X_{\rm CH4}$ posteriors recover the expected values; however, the true $X_{\rm CH4}$ values often fall outside the posterior credible intervals. As the orbital phase approaches the hot-spot longitude, $X_{\rm CH4}$ drops below spectroscopically detectable values. Despite this significant decrease, the disk-integrated analysis shows tightly constrained $X_{\rm CH4}$ posteriors that overestimate the true values by several orders of magnitude. This clear mismatch is reminiscent of the CH_4 biases found by Feng et al. (2016, 2020). The longitudinally resolved analysis effectively recovered $X_{\rm CH4}$ upper limits at the four orbital phases around the hot-spot longitude, but did not fit well the abundances around first- and third-quarter phases. This bias

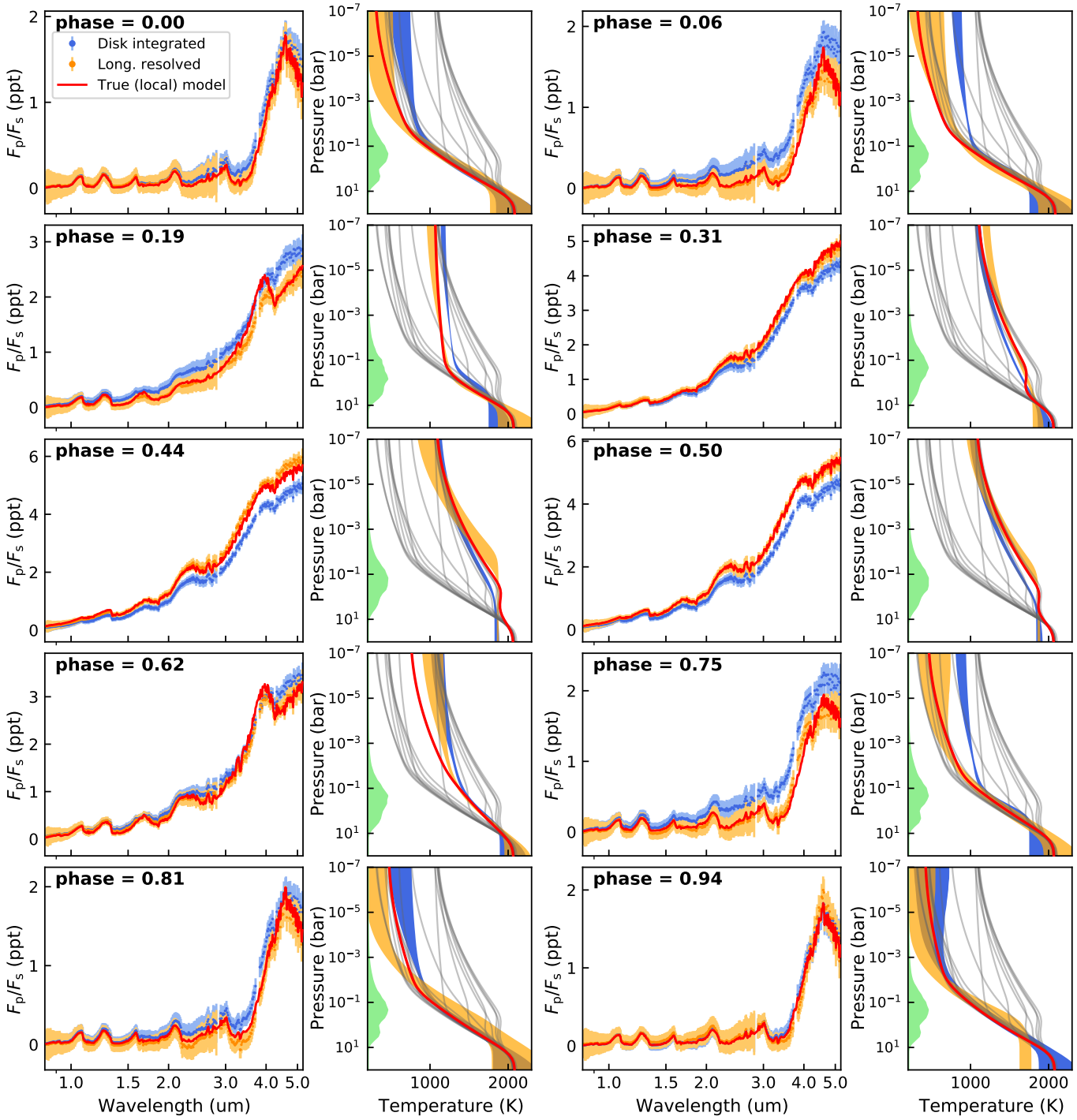

Figure 6. Model and retrieval of the synthetic WASP-43b *JWST* phase-curve observation of the variable-composition case (M2). Each pair of panels show the model spectra and retrieved temperature profiles at selected orbital phases (see labels). The disk-integrated and longitudinally resolved analyses are denoted by the blue and orange colors, respectively. The red curves denote local spectra and temperature profiles at the sub-observer longitude of each orbital phase. The gray curves denote the temperature profiles of the true model at all longitudinal slices. The width of the green curve denotes the relative contribution function at each pressure level for these *JWST* simulations.

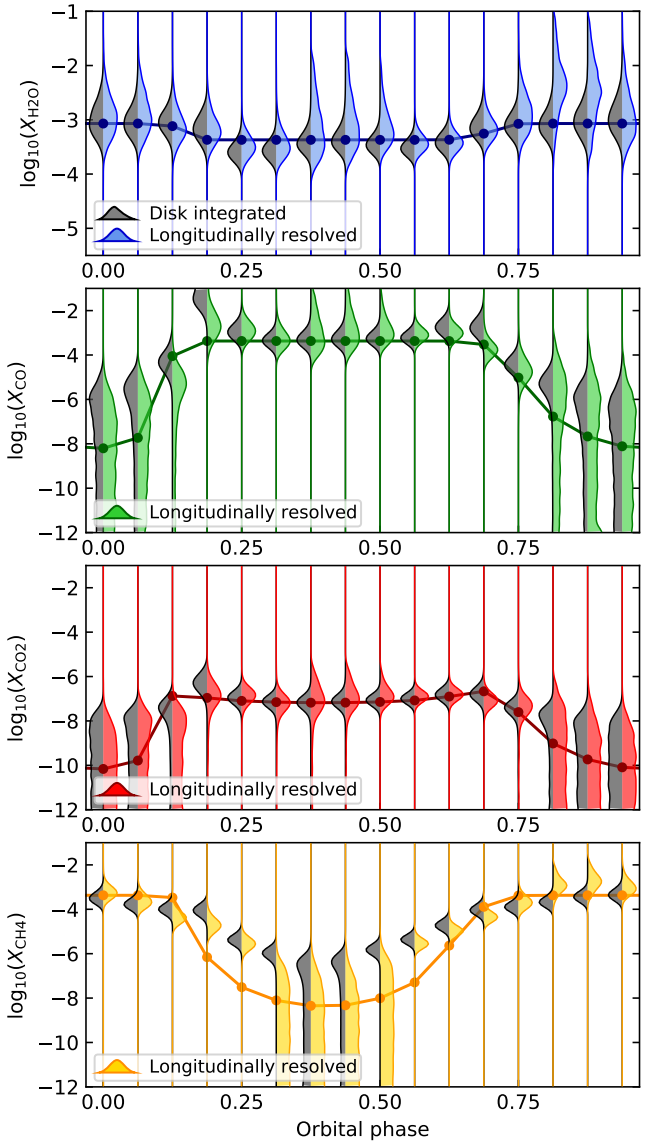

Figure 7. Retrieved WASP-43b volume-mixing ratios of the synthetic WASP-43b *JWST* phase-curve observation of the variable-composition case (M2). The gray and colored histograms show the posterior distributions of the disk-integrated and longitudinally resolved analyses, respectively, as a function of orbital phase. The marginal posteriors have been smoothed for better visualization. The solid curves with dot markers denote the input abundances at the sub-observer longitudes corresponding to each orbital phase.

is significantly more severe than for CO or CO_2. In any case, it should be noted that our simulated observations presume local-thermochemical equilibrium, whereas horizontal quenching can drive the atmosphere towards longitudinally uniform abundances (Cooper & Showman 2006).

To quantify whether the longitudinally resolved retrievals improved the volume-mixing ratio estimation over the disk-integrated retrievals, we computed the Z-scores between the true volume mixing ratios and the marginal posterior distributions. For a distribution with standard deviation σ and mean μ, the Z-score of a datum x is its distance from the mean in units of the standard deviation, $z = (x-\mu)/\sigma$. Since the posteriors are often asymmetric and we are interested in the maximum *a posteriori* estimation, we computed the Z-scores using the mode of the posteriors. Table 4 presents the retrieval Z-score (average of the Z-score absolute values over all orbital phases) for each molecule and dataset. The Z-scores show that the longitudinally resolved analysis clearly improves the retrieval of $X_{\rm CO}$ and $X_{\rm CH4}$ (i.e., Z-scores closer to zero). For the other two molecules, both analyzes perform relatively well (Z-scores < 1.0), and the Z-score differences are small between the longitudinally resolved and disk-integrated analyses.

Table 4. Retrieval Z-score Statistics

	$X_{\rm H2O}$	$X_{\rm CO}$	$X_{\rm CO2}$	$X_{\rm CH4}$	Approach
Z-score	0.50	1.15	0.72	4.56	disk-integrated
Z-score	**0.41**	**0.69**	**0.53**	**2.76**	long. resolved

4. Discussion

4.1. *Longitudinally Resolved Spectral Retrieval: the Good, the Bad and the Ugly*

We have shown that longitudinally resolved spectral retrieval is preferable to disk-integrated retrieval: when measurement uncertainties are large the two approaches are equivalent, but for high signal-to-noise observations it yields significantly different atmospheric properties that are more accurate than disk-integrated spectral retrieval. Moreover, our approach is compatible with off-the-shelf 1D spectral retrieval models and hence is complementary to efforts by other groups to develop multi-dimensional spectral retrieval codes (Caldas et al. 2019; Irwin et al. 2020; Taylor et al. 2020; Feng et al. 2020). While it may seem strange to perform spectral retrieval on a reconstructed spectrum that was never directly observed, this is conceptually similar to the data reduction and decorrelation required for most exoplanet spectroscopy.

It should be emphasized that phase mapping is always an under-constrained problem, regardless of the adopted parameterization. The best one can do is quantify the degeneracies and how they impact the astrophysical uncertainties. For example, Beatty et al. (2019) suggested that certain phase curves are more efficiently fit with a different map parameterization. If the brightness map of a planet includes sharp transitions then a map parameterization involving uniform longitudinal slices (cf. Knutson et al. 2007) may provide an acceptable fit with fewer parameters than the Fourier mapping approach adopted in this paper (see updated discussion of mapping parameterization in Cowan & Fujii 2018).

Marginalizing over different mapping parameterizations like sinusoids, slices, or the step function from Beatty et al. (2019) would require a reversible jump MCMC. Alternatively, a pixel- or slice-based map regularized with a Gaussian process can retrieve the map and length scale of brightness variations (Farr et al. 2018). However, any periodic

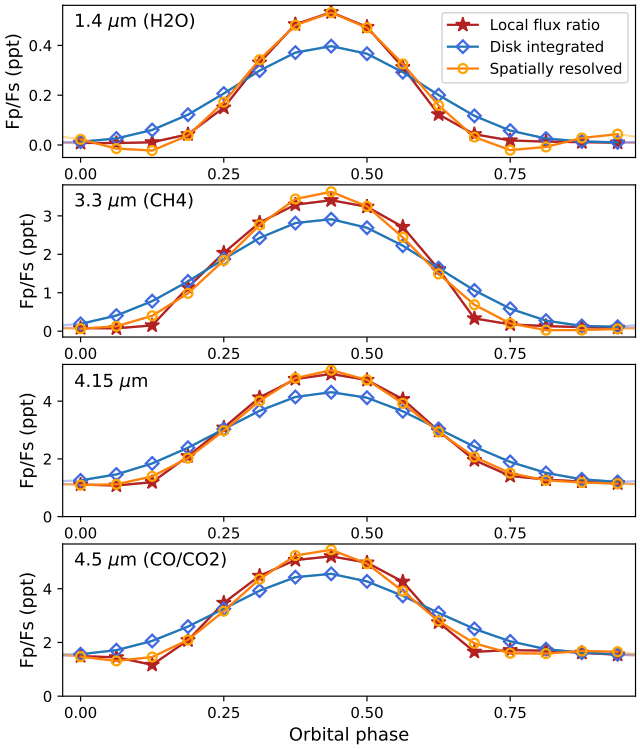

Figure 8. WASP-43b model phase curves at selected wavelengths, where the spectrum is dominated by H_2O (1.4 μm), CH_4 (3.3 μm), by no particular molecule (4.15 μm), and CO/CO_2 (4.5 μm). The longitudinally resolved dataset matches much better the phase curve assuming local properties at each phase than the disk-integrated dataset. However, the spectral mapping is not perfect, in particular, it does not perform well at first and third quadrature, this is consistent with these phases being the most problematic for the atmospheric retrievals.

function can be represented by a Fourier series, it is just a question of the order of the expansion.

We have tested whether the data favour sharp discontinuities by performing fits with different orders of Fourier series to our more realistic simulated WASP-43b observations (M2 phase-curve model): maps with sharp turns or discontinuities (Figure 8) produce light curves with significant power in high-frequency Fourier modes. The Information Criteria suggest that second-order sinusoidal light curve models were favoured over lower and higher order models.

For the second order Fourier series we adopt throughout this paper, one can extract approximately four independent longitudinally resolved spectra. Spectra at longitudes less than 90 degrees from each other will be more or less correlated. This correlation is dictated by the disk-integration rather than the specific map parameterization: a pixel-based map with more than four slices would exhibit similar correlations.

4.2. *Fourier Odd Harmonics*

For a planet on a circular edge-on orbit, symmetry dictates that odd order harmonics present in the longitudinal brightness map are not visible in the corresponding phase curve (Cowan & Agol 2008). Significant North-South asymmetry in the temperature map could make odd harmonics visible in the phase variations of a non-edge-on planet (Cowan et al. 2017), but most odd modes of the map have no lightcurve signature, regardless of inclination (Cowan et al. 2013). The odd-mode degeneracy affects all map parameterizations: the addition of odd longitudinal modes to any brightness map will not change the resulting disk-integrated phase variations.

Since we simulated the WASP-43b observations using results from a GCM, we know what the "true" longitudinal maps look like. To quantify how much the odd mode degeneracy could affect spectral mapping, we fit the longitudinal maps from the WASP-43b GCM results directly, and tested various order Fourier series like we did for the phase curves (as in §4.1). This time, a third order model was favoured over a second order model. The first and second order amplitudes and offsets were the same between the two models, because sinusoids of various orders form an orthogonal basis. Averaged over wavelengths, the third order amplitude was just 9% of the first order amplitude for the simulated data. Both the second-order and third-order maps provide good fits to the true maps, matching within the map uncertainties. This suggests that, for a realistic GCM, the third order degeneracy is not introducing an appreciable bias.

4.3. *When is Longitudinally Resolved Spectral Retrieval Preferable to Disk-Integrated Retrieval?*

The numerical experiments in §3.3 and §3.4 show that longitudinally resolved spectral retrieval is more accurate than disk-integrated 1D retrieval, as expected. But for the *HST*/WFC3 and *Spitzer*/IRAC phase curves of WASP-43b (Stevenson et al. 2014, 2017) we found no significant difference in the WASP-43b abundances between the spatially resolved and the hemispheric integrated retrievals (§2). This is unsurprising since the longitudinally-resolved and hemispherically-averaged spectra overlap with each other within the 1σ uncertainties (Figure 1). In other words, the uncertainties are so large for these data that there is minimal benefit—but also no harm— in performing a spatially resolved retrieval over a hemispheric integration. In Appendix A we derive an analytic expression for the longitudinal map uncertainties as a function of the uncertainties in the spectral phase curve, and in Appendix B we derive an expression for the difference between a phase curve and the corresponding map, a metric for the utility of the longitudinally resolved spectral retrieval approach.

4.4. *Longitudinally Resolved Spectral Retrieval of Brown Dwarfs*

While the focus on this paper has been on spatially resolved-retrieval of transiting exoplanets, this method can in principle also be applied to variable brown dwarfs and directly-imaged exoplanets. Such an analysis could reveal the properties of clouds that drive the observed variability. Brown dwarfs and wide-orbit companions are known to exhibit cloud-driven variability with amplitudes as high as ∼25% in the near-infrared (Radigan et al. 2012; Bowler et al. 2020). However, the temperature contrast between

cloud layers in brown dwarf atmospheres is estimated to be a few hundred K (Apai et al. 2013), much smaller than the temperature contrast between the day and night side of short-period exoplanets. Another challenge for brown dwarfs is that the clouds responsible for variability can evolve rapidly (e.g Apai et al. 2017; Vos et al. 2018) so *simultaneous* multi-band monitoring is necessary. Very few brown dwarfs were monitored simultaneously with *HST* and *Spitzer* (Biller et al. 2018; Buenzli et al. 2012). Our preliminary attempts using these simultaneous data did not yield significant differences in the longitudinally-resolved spectra. As with the hot Jupiter WASP-43b, we expect that observations of variable brown dwarfs with *JWST* may benefit from longitudinally resolved spectral retrieval.

5. Conclusions

Accounting for the multi-dimensional nature of planets represents an open challenge for the exoplanet retrieval community, and a significant step up in complexity, relative to 1D models. 3D models not only are more computationally demanding, but have more complex parameter spaces that are harder to interpret. Even model validation becomes non trivial, while too-complex models can become easily intractable under a retrieval framework, too-simple models might fail to capture the inhomogeneities predicted by self-consistent physical models. Taylor et al. (2020) and Feng et al. (2020) have shown that linear-combination models can improve the accuracy of atmospheric retrievals under the assumption of globally constant composition and a two-component (day and night side) temperature profile. However, assessing how these methods fare against a smoother longitudinal variation of temperature and composition remains to be investigated. In contrast, our longitudinally resolved approach is expected to perform better for a planet where the physical properties vary smoothly with longitude (as predicted by GCMs) than for a discrete two-hemispheric model. Furthermore, a key advantage of the longitudinally resolved approach is that it provides significant gains in accuracy of the retrieved thermal structure over disk-integrated retrievals via an easy pre-processing step to existing 1D retrieval codes.

As found here and in other multi-dimensional studies, retrieving accurate exoplanet compositions remains challenging. Longitudinally resolved retrievals provide marked improvement over disk-integrated retrievals, although both struggle with CH_4; presumably due to its limited impact in a spectrum dominated by H_2O features, and its fast variation in composition between day (depleted) and night side (plentiful). Feng et al. (2020) and Taylor et al. (2020) found the CH_4 abundance particularly biased when applying the traditional 1D disk-integrated analysis. Using their inhomogeneous two-component models they correctly recover the expected upper-limit constraint on CH_4; however, they generated their input synthetic models assuming globally uniform abundances (both in pressure and longitude), a simpler problem than the ones tackled in our study and hence less liable to biases. The longitudinal variation of minor species like CH_4 probes the degree to which horizontal quenching can drive atmospheres towards longitudinally uniform abundances. Thus, properly understanding the biases in these estimations is fundamental to assess the dynamical properties of exoplanets.

Future missions will enable exoplanet atmospheric characterization with unprecedented detail, but at the same time they will expose the multiple shortcomings of present-day retrieval models that have so far remained under the radar. In this article we found that longitudinally resolved spectral retrieval can improve the temperature and composition estimation of inhomogeneous planets observed with the *James Webb Space Telescope*.

We have made available the data and analysis used in this article at https://doi.org/10.5281/zenodo.4757164

This project was conceived at the "Multi-dimensional characterization of distant worlds: spectral retrieval and spatial mapping" workshop hosted by the Michigan Institute for Research in Astrophysics and spearheaded by Emily Rauscher. We thank the anonymous referee for his/her time and valuable comments. We thank contributors to the Python Programming Language and the free and open-source community (see Software Section below). We drafted this article using the AASTeX6.2 latex template (AAS Journals Team & Hendrickson 2018), with further style modifications that are available at https://github.com/pcubillos/ApJtemplate. Part of this work is based based on observations made with the NASA/ESA Hubble Space Telescope, obtained from the data archive at the Space Telescope Science Institute. STScI is operated by the Association of Universities for Research in Astronomy, Inc. under NASA contract NAS 5-26555. This work is based in part on observations made with the *Spitzer Space Telescope*, which is operated by the Jet Propulsion Laboratory, California Institute of Technology under a contract with NASA. This research has made use of NASA's Astrophysics Data System Bibliographic Services. D. K. and N. B. C. acknowledge support from McGill Space Institute and the Institute for Research on Exoplanets. E. G. acknowledges support for this work by the NSF under Grant No. AST-1614527 and Grant No. AST-1313278, by NASA under *Kepler* Grant No. 80NSSC19K0106, and the LSSTC Data Science Fellowship Program, which is funded by LSSTC, NSF Cybertraining Grant No. 1829740, the Brinson Foundation, and the Moore Foundation; her participation in the program has benefited this work.

Software:

PYRAT BAY (Cubillos & Blecic 2021), MC3 (Cubillos et al. 2017), RATE (Cubillos et al. 2019), REPACK (Cubillos 2017), NUMPY (Harris et al. 2020), SCIPY (Virtanen et al. 2020), SYMPY (Meurer et al. 2017), ASTROPY (Astropy Collaboration et al. 2013, 2018), PYMC3 (Salvatier et al. 2016), MATPLOTLIB (Hunter 2007), IPYTHON (Pérez & Granger 2007), AASTeX6.2 (AAS Journals Team & Hendrickson 2018), and BIBMANAGER[3] (Cubillos 2019).

[3] http://pcubillos.github.io/bibmanager

References

AAS Journals Team, & Hendrickson, A. 2018, Aasjournals/Aastex60: Version 6.2 Official Release, ADS

Agúndez, M., Venot, O., Iro, N., Selsis, F., Hersant, F., Hébrard, E., & Dobrijevic, M. 2012, A&A, 548, A73, ADS, 1210.6627

Andrae, R. 2010, arXiv e-prints, arXiv:1009.2755, ADS, 1009.2755

Apai, D. et al. 2017, Science, 357, 683, ADS

Apai, D., Radigan, J., Buenzli, E., Burrows, A., Reid, I. N., & Jayawardhana, R. 2013, ApJ, 768, 121, ADS, 1303.4151

Asplund, M., Grevesse, N., Sauval, A. J., & Scott, P. 2009, ARA&A, 47, 481, ADS, 0909.0948

Astropy Collaboration et al. 2018, AJ, 156, 123, ADS, 1801.02634

Astropy Collaboration et al. 2013, A&A, 558, A33, ADS, 1307.6212

Batalha, N. E. et al. 2017, PASP, 129, 064501, ADS, 1702.01820

Beatty, T. G., Marley, M. S., Gaudi, B. S., Colón, K. D., Fortney, J. J., & Showman, A. P. 2019, AJ, 158, 166, ADS, 1808.09575

Bell, T. J., & Cowan, N. B. 2018, ApJL, 857, L20, ADS, 1802.07725

Biller, B. A. et al. 2018, AJ, 155, 95, ADS, 1712.03746

Blecic, J., Dobbs-Dixon, I., & Greene, T. 2017, ApJ, 848, 127, ADS, 1803.06678

Blecic, J. et al. 2014, ApJ, 781, 116, ADS, 1302.7003

Borysow, A. 2002, A&A, 390, 779, ADS

Borysow, A., & Frommhold, L. 1989, ApJ, 341, 549, ADS

Borysow, A., Frommhold, L., & Moraldi, M. 1989, ApJ, 336, 495, ADS

Borysow, A., Jorgensen, U. G., & Fu, Y. 2001, JQSRT, 68, 235, ADS

Borysow, J., Frommhold, L., & Birnbaum, G. 1988, ApJ, 326, 509, ADS

Bowler, B. P., Zhou, Y., Morley, C. V., Kataria, T., Bryan, M. L., Benneke, B., & Batygin, K. 2020, ApJL, 893, L30, ADS, 2004.05170

Buenzli, E. et al. 2012, ApJL, 760, L31, ADS, 1210.6654

Caldas, A., Leconte, J., Selsis, F., Waldmann, I. P., Bordé, P., Rocchetto, M., & Charnay, B. 2019, A&A, 623, A161, ADS, 1901.09932

Castelli, F., & Kurucz, R. L. 2003, in Modelling of Stellar Atmospheres, ed. N. Piskunov, W. W. Weiss, & D. F. Gray, Vol. 210, A20, astro-ph/0405087, ADS

Cooper, C. S., & Showman, A. P. 2006, ApJ, 649, 1048, ADS, astro-ph/0602477

Cowan, N. B., & Agol, E. 2008, ApJL, 678, L129, ADS, 0803.3622

Cowan, N. B., Chayes, V., Bouffard, É., Meynig, M., & Haggard, H. M. 2017, MNRAS, 467, 747, ADS, 1611.05925

Cowan, N. B., Fuentes, P. A., & Haggard, H. M. 2013, MNRAS, 434, 2465, ADS, 1304.6398

Cowan, N. B., & Fujii, Y. 2018, Mapping Exoplanets, ed. H. J. Deeg & J. A. Belmonte, 147, ADS

Cubillos, P., Harrington, J., Loredo, T. J., Lust, N. B., Blecic, J., & Stemm, M. 2017, AJ, 153, 3, ADS, 1610.01336

Cubillos, P. E. 2017, ApJ, 850, 32, ADS, 1710.02556

Cubillos, P. E. 2019, bibmanager: A BibTeX manager for LaTeX projects, Zenodo, doi:10.5281/zenodo.2547042, ADS

Cubillos, P. E. 2021, ApJS, submitted.

Cubillos, P. E., & Blecic, J. 2021, arXiv e-prints, arXiv:2105.05598, ADS, 2105.05598

Cubillos, P. E., Blecic, J., & Dobbs-Dixon, I. 2019, ApJ, 872, 111, ADS, 1901.03764

Dobbs-Dixon, I., & Cowan, N. B. 2017, ApJL, 851, L26, ADS, 1711.08463

Farr, B., Farr, W. M., Cowan, N. B., Haggard, H. M., & Robinson, T. 2018, AJ, 156, 146, ADS, 1802.06805

Feng, Y. K., Line, M. R., & Fortney, J. J. 2020, AJ, 160, 137, ADS, 2006.11442

Feng, Y. K., Line, M. R., Fortney, J. J., Stevenson, K. B., Bean, J., Kreidberg, L., & Parmentier, V. 2016, ApJ, 829, 52, ADS, 1607.03230

Feng, Y. K., Robinson, T. D., Fortney, J. J., Lupu, R. E., Marley, M. S., Lewis, N. K., Macintosh, B., & Line, M. R. 2018, AJ, 155, 200, ADS, 1803.06403

Gelman, A., & Rubin, D. B. 1992, Statistical Science, 7, 457, ADS

Gillon, M. et al. 2012, A&A, 542, A4, ADS, 1201.2789

Greene, T. P., Line, M. R., Montero, C., Fortney, J. J., Lustig-Yaeger, J., & Luther, K. 2016, ApJ, 817, 17, ADS, 1511.05528

Guillot, T. 2010, A&A, 520, A27, ADS, 1006.4702

Harris, C. R. et al. 2020, Nature, 585, 357, ADS, 2006.10256

Hellier, C. et al. 2011, A&A, 535, L7, ADS, 1104.2823

Hunter, J. D. 2007, Computing In Science & Engineering, 9, 90

Irwin, P. G. J., Parmentier, V., Taylor, J., Barstow, J., Aigrain, S., Lee, G. K. H., & Garland, R. 2020, MNRAS, 493, 106, ADS, 1909.03233

Kataria, T., Showman, A. P., Fortney, J. J., Stevenson, K. B., Line, M. R., Kreidberg, L., Bean, J. L., & Désert, J.-M. 2015, ApJ, 801, 86, ADS, 1410.2382

Keating, D., & Cowan, N. B. 2017, ApJL, 849, L5, ADS, 1709.03502

Knutson, H. A. et al. 2007, Nature, 447, 183, ADS, 0705.0993

Knutson, H. A. et al. 2009, ApJ, 690, 822, ADS, 0802.1705

Knutson, H. A. et al. 2012, ApJ, 754, 22, ADS, 1206.6887

Kreidberg, L. et al. 2014, ApJL, 793, L27, ADS, 1410.2255

Lecavelier Des Etangs, A., Pont, F., Vidal-Madjar, A., & Sing, D. 2008, A&A, 481, L83, ADS, 0802.3228

Léger, A. et al. 2011, Icarus, 213, 1, ADS, 1102.1629

Li, G., Gordon, I. E., Rothman, L. S., Tan, Y., Hu, S.-M., Kassi, S., Campargue, A., & Medvedev, E. S. 2015, ApJS, 216, 15, ADS

Line, M. R. et al. 2013, ApJ, 775, 137, ADS, 1304.5561

Louden, T., & Kreidberg, L. 2018, MNRAS, 477, 2613, ADS, 1711.00494

Madhusudhan, N., & Seager, S. 2009, ApJ, 707, 24, ADS, 0910.1347

Mai, C., & Line, M. R. 2019, ApJ, 883, 144, ADS, 1908.10904

Mendonça, J. M., Malik, M., Demory, B.-O., & Heng, K. 2018, AJ, 155, 150, ADS, 1802.03047

Meurer, A. et al. 2017, PeerJ Computer Science, 3, e103

Parmentier, V., & Crossfield, I. J. M. 2018, Exoplanet Phase Curves: Observations and Theory, ed. H. J. Deeg & J. A. Belmonte, 116, ADS

Parmentier, V., Fortney, J. J., Showman, A. P., Morley, C., & Marley, M. S. 2016, ApJ, 828, 22, ADS, 1602.03088

Parmentier, V., Showman, A. P., & Fortney, J. J. 2021, MNRAS, 501, 78, ADS, 2010.06934

Pérez, F., & Granger, B. E. 2007, Computing in Science and Engineering, 9, 21

Polyansky, O. L., Kyuberis, A. A., Zobov, N. F., Tennyson, J., Yurchenko, S. N., & Lodi, L. 2018, MNRAS, 480, 2597, ADS, 1807.04529

Pontoppidan, K. M. et al. 2016, in Society of Photo-Optical Instrumentation Engineers (SPIE) Conference Series, Vol. 9910, Observatory Operations: Strategies, Processes, and Systems VI, ed. A. B. Peck, R. L. Seaman, & C. R. Benn, 991016, 1707.02202, ADS

Radigan, J., Jayawardhana, R., Lafrenière, D., Artigau, É., Marley, M., & Saumon, D. 2012, ApJ, 750, 105, ADS, 1201.3403

Rodgers, C. D. 2000, Inverse Methods for Atmospheric Sounding: Theory and Practice, ADS

Roman, M. T., Kempton, E. M. R., Rauscher, E., Harada, C. K., Bean, J. L., & Stevenson, K. B. 2021, ApJ, 908, 101, ADS, 2010.06936

Rothman, L. S. et al. 2010, JQSRT, 111, 2139, ADS

Salvatier, J., Wiecki, T. V., & Fonnesbeck, C. 2016, PyMC3: Python probabilistic programming framework, 1610.016, ADS

Schwartz, J. C., & Cowan, N. B. 2015, MNRAS, 449, 4192, ADS, 1502.06970

Schwarz, G. 1978, Annals of Statistics, 6, 461, ADS

Showman, A. P., & Guillot, T. 2002, A&A, 385, 166, ADS, astro-ph/0202236

Stevenson, K. B. et al. 2014, Science, 346, 838, ADS, 1410.2241

Stevenson, K. B. et al. 2017, AJ, 153, 68, ADS, 1608.00056

Tan, X., & Komacek, T. D. 2019, ApJ, 886, 26, ADS, 1910.01622

Taylor, J., Parmentier, V., Irwin, P. G. J., Aigrain, S., Lee, G. K. H., & Krissansen-Totton, J. 2020, MNRAS, 493, 4342, ADS, 2002.00773

ter Braak, C. J. F., & Vrugt, J. A. 2008, Statistics and Computing, 18, 435

Venot, O. et al. 2020, ApJ, 890, 176, ADS, 2001.04759

Virtanen, P. et al. 2020, Nature Methods, 17, 261, ADS, 1907.10121
Vos, J. M., Allers, K. N., Biller, B. A., Liu, M. C., Dupuy, T. J., Gallimore, J. F., Adenuga, I. J., & Best, W. M. J. 2018, MNRAS, 474, 1041, ADS, 1710.07194
Watanabe, S. 2010, arXiv e-prints, arXiv:1004.2316, ADS, 1004.2316
Yurchenko, S. N., & Tennyson, J. 2014, MNRAS, 440, 1649, ADS, 1401.4852

Appendix

A. Analytic phase mapping

In order to most easily invert the phase variations into maps, we would like to parameterize the wavelength-dependent phase variations as a Fourier series, following Cowan & Agol (2008):

$$F(\xi,\lambda) = F_0(\lambda) + C_1(\lambda)\cos\xi + D_1(\lambda)\sin\xi + C_2(\lambda)\cos(2\xi) + D_2(\lambda)\sin(2\xi) + \ldots \quad \text{(A1)}$$

where ξ is the orbital phase from superior conjunction ($\xi = 0$ at eclipse, $\xi = \pi$ at transit). High-order harmonics are suppressed quadratically in the phase curve (e.g., the 4ξ modes are $4\times$ smaller than the 2ξ modes, given the same map amplitude) and the odd harmonics (3ξ, 5ξ, etc.) are invisible for an edge-on-planet due to symmetry (Cowan et al. 2013), so most authors have limited themselves to a second-order Fourier expansion.

In order to ensure that our spatially resolved spectra have the same normalization as the disk-integrated spectra, we multiply the longitudinal map expressions from Cowan & Agol (2008) by 2. To second order, the longitudinal planet map is therefore:

$$\tilde{J}(\phi,\lambda) = F_0(\lambda) + \frac{4}{\pi}C_1(\lambda)\cos\phi - \frac{4}{\pi}D_1(\lambda)\sin\phi + 3C_2(\lambda)\cos(2\phi) - 3D_2(\lambda)\sin(2\phi), \quad \text{(A2)}$$

where ϕ is the planetary longitude, with the convention that $\phi = 0$ at the sub-stellar point and increases to the East (the direction of synchronous rotation).[4]

Omitting the wavelength dependence for clarity, the uncertainty in the phase curve is

$$\sigma_{F_\xi} = \sigma_{F_0} + \sigma_{C_1}\cos\xi + \sigma_{D_1}\sin\xi + \sigma_{C_2}\cos(2\xi) + \sigma_{D_2}\sin(2\xi), \quad \text{(A3)}$$

while the uncertainty in the corresponding longitudinal map is

$$\sigma_{J_\phi} = \sigma_{F_0} + \frac{4}{\pi}\sigma_{C_1}\cos\phi - \frac{4}{\pi}\sigma_{D_1}\sin\phi + 3\sigma_{C_2}\cos(2\phi) - 3\sigma_{D_2}\sin(2\phi). \quad \text{(A4)}$$

B. Difference Between the Resolved Map and the Phase Curve

Making the substitution $\xi = -\phi$ in Eq. (A1) yields the disk-integrated brightness of the planet when the longitude ϕ is facing the observer, i.e., a phase curve that can be directly compared to the planet's longitudinal map. The shape of the longitudinal map differs significantly from that of the phase curve if $|\delta(\phi,\lambda)|/\sigma_\delta(\phi) > 1$, where the difference is

$$\begin{aligned}\delta(\phi,\lambda) &\equiv \tilde{J}(\phi,\lambda) - F(-\phi,\lambda)\\ &= \left(\frac{4}{\pi} - 1\right)\Big[C_1(\lambda)\cos\phi - D_1(\lambda)\sin\phi\Big]\\ &\quad + 2\Big[C_2(\lambda)\cos(2\phi) - D_2(\lambda)\sin(2\phi)\Big] \quad \text{(B5)}\end{aligned}$$

and its uncertainty is

$$\begin{aligned}\sigma_\delta^2(\phi) &= \left(\frac{4}{\pi} - 1\right)^2\Big[\sigma_{C_1}^2\cos^2\phi + \sigma_{D_1}^2\sin^2\phi\Big]\\ &\quad + 4\Big[\sigma_{C_2}^2\cos^2(2\phi) + \sigma_{D_2}^2\sin^2(2\phi)\Big], \quad \text{(B6)}\end{aligned}$$

where we have again omitted the wavelength-dependence for clarity. In other words, the longitudinal map has a significantly different shape from the phase curve if

$$\frac{|\delta(\phi,\lambda)|}{\sigma_\delta(\phi)} > 1. \quad \text{(B7)}$$

Note the absence of the mean spectrum of the planet, $F_0(\lambda)$, and its uncertainty, σ_{F_0} from this expression.

In practice, spectral retrieval can only be performed on spectra, not the difference of spectra. In other words, uncertainties in the eclipse spectrum, largely responsible for constraining $F_0(\lambda)$, can make longitudinally resolved spectra consistent with disk-integrated spectra. As such, a more salient metric is $|\delta(\phi,\lambda)|/\sigma_\Delta(\phi) > 1$, where

$$\begin{aligned}\sigma_\Delta^2(\phi) &= \sigma_{F(-\phi)}^2 + \sigma_{\tilde{J}(\phi)}^2\\ &= \Big[\sigma_{F_0} + \sigma_{C_1}\cos\phi + \sigma_{D_1(\lambda)}\sin\phi\\ &\quad + \sigma_{C_2}\cos(2\phi) + \sigma_{D_2}(\lambda)\sin(2\phi)\Big]^2\\ &\quad \Big[\sigma_{F_0} + \frac{4}{\pi}\sigma_{C_1}\cos\phi - \frac{4}{\pi}\sigma_{D_1}\sin\phi\\ &\quad + 3\sigma_{C_2}\cos(2\phi) - 3\sigma_{D_2}(\lambda)\sin(2\phi)\Big]^2, \quad \text{(B8)}\end{aligned}$$

where we have again omitted the wavelength-dependence for clarity. Given an observed phase curve parameterized in terms of C_1, C_2, D_1, D_2 and their uncertainties, it is a simple matter to check whether the difference between the longitudinal map and the lightcurve is significant.

C. Converting Between Phase Curve Parameterizations

Instead of the phase curve parameterization above, Stevenson et al. (2014, 2017) report the eclipse depth, cosine amplitude(s), and the corresponding phase offset(s). In particular, for the HST/WFC3 spectrally resolved phase curves, Stevenson et al. (2014) use the functional form

$$F(t,\lambda) = F_0(\lambda) + c_1(\lambda)\cos\left(\frac{2\pi}{P}\Big[(t - t_e) - \Delta t(\lambda)\Big]\right), \quad \text{(C9)}$$

[4] These maths were derived for an equator-on viewing geometry and hence should be accurate for a transiting planet like WASP-43b (the general solution is presented in Cowan et al. 2013).

where t_e is the time of eclipse and $\Delta t(\lambda)$ is the phase offset from eclipse in minutes. For Spitzer/IRAC phase curves, Stevenson et al. (2017) adopt a second order Fourier series and use a different convention for the phase offset:

$$F(t,\lambda) = F_0(\lambda) + c_1(\lambda)\cos\left(\frac{2\pi}{P}\Big[t - c_2(\lambda)\Big]\right) + c_3(\lambda)\cos\left(\frac{4\pi}{P}\Big[t - c_4(\lambda)\Big]\right). \quad \text{(C10)}$$

In the equations above, t is time and P is the planet's orbital period. We can instead express this in terms of orbital phase, $\xi = 2\pi(t - t_e)/P$, omitting the wavelength-dependence of the coefficients for clarity:

$$F(\xi) = F_0 + c_1\cos(\xi - \xi_1) + c_3\cos(2(\xi - \xi_3)), \quad \text{(C11)}$$

where $\xi_1 = 2\pi(c_2 - t_e)/P$ and $\xi_3 = 2\pi(c_4 - t_e)/P$. Using trigonometric identities, we get expressions for the Fourier coefficients, $C_1 = c_1\cos\xi_1$, $D_1 = c_1\sin\xi_1$, $C_2 = c_3\cos(2\xi_3)$, $D_2 = c_3\sin(2\xi_3)$, and their uncertainties:

$$\sigma_{C_1}^2 = \sigma_{c_1}^2\cos^2\xi_1 + \sigma_{\xi_1}^2 c_1^2\sin^2\xi_1 \quad \text{(C12)}$$

$$\sigma_{D_1}^2 = \sigma_{c_1}^2\sin^2\xi_1 + \sigma_{\xi_1}^2 c_1^2\cos^2\xi_1 \quad \text{(C13)}$$

$$\sigma_{C_2}^2 = \sigma_{c_3}^2\cos^2(2\xi_3) + 4\sigma_{\xi_3}^2 c_3^2\sin^2(2\xi_3) \quad \text{(C14)}$$

$$\sigma_{D_2}^2 = \sigma_{c_3}^2\sin^2(2\xi_3) + 4\sigma_{\xi_3}^2 c_3^2\cos^2(2\xi_3), \quad \text{(C15)}$$

and finally the phase offsets: $\sigma_{\xi_1} = \frac{2\pi}{P}\sigma_{c_2}$ and $\sigma_{\xi_3} = \frac{2\pi}{P}\sigma_{c_4}$, where we presume that the relative uncertainty on the eclipse time and orbital period are negligible compared to the relative uncertainty on the phase offset.